JGR Oceans

RESEARCH ARTICLE
10.1029/2022JC019103

**Key Points:**

- First observations with an Autonomous Underwater Vehicle beneath Ronne Ice Shelf, Antarctica, along the Modified Warm Deep Water inflow path
- The inflow velocity averages 4 cm $s^{-1}$, and the hydrographic properties show strong spatial variability that is subject to tidal advection
- Turbulent mixing is elevated for the warmest Modified Warm Deep Water, with eddy diffusivity values reaching $10^{-4}$ $m^2$ $s^{-1}$

**Supporting Information:**

Supporting Information may be found in the online version of this article.

**Correspondence to:**

P. E. D. Davis,
petvis@bas.ac.uk

**Citation:**

Davis, P. E. D., Jenkins, A., Nicholls, K. W., Dutrieux, P., Schröder, M., Janout, M. A., et al. (2022). Observations of Modified Warm Deep Water beneath Ronne Ice Shelf, Antarctica, from an Autonomous Underwater Vehicle. *Journal of Geophysical Research: Oceans*, *127*, e2022JC019103. https://doi.org/10.1029/2022JC019103

Received 19 JUL 2022
Accepted 17 OCT 2022



# Observations of Modified Warm Deep Water Beneath Ronne Ice Shelf, Antarctica, From an Autonomous Underwater Vehicle

**Peter E. D. Davis[1], Adrian Jenkins[2], Keith W. Nicholls[1], Pierre Dutrieux[1], Michael Schröder[3], Markus A. Janout[3], Hartmut H. Hellmer[3], Rob Templeton[4], and Stephen McPhail[4]**

[1]British Antarctic Survey, Natural Environment Research Council, Cambridge, UK, [2]Department of Geography and Environmental Sciences, Faculty of Engineering and Environment, Northumbria University, Newcastle upon Tyne, UK, [3]Alfred-Wegener-Institute Helmholtz Centre for Polar and Marine Research, Bremerhaven, Germany, [4]Marine Autonomous and Robotic Systems, National Oceanography Centre, Southampton, UK

**Abstract** Filchner-Ronne Ice Shelf (FRIS) is the world's largest ice shelf by volume. It helps regulate Antarctica's contribution to global sea level rise, and water mass transformations within the sub-ice-shelf cavity produce globally important dense water masses. Rates of ice shelf basal melting are relatively low, however, as the production of cold (−1.9°C) and dense High Salinity Shelf Water over the Weddell Sea continental shelf isolates the ice shelf from large-scale inflow of warm water. Nevertheless, a narrow inflow of relatively warm (−1.4°C) Modified Warm Deep Water (MWDW) that hugs the western flank of Berkner Bank is observed to reach Ronne Ice Front, although the processes governing its circulation and fate remain uncertain. Here we present the first observations taken within the ice shelf cavity along this warm water inflow using the Autosub Long Range autonomous underwater vehicle. We observe a core of MWDW with a south-westward velocity of 4 cm $s^{-1}$ that reaches at least 18 km into the sub-ice cavity. The hydrographic properties are spatially heterogeneous, giving rise to temporal variability that is driven by tidal advection. The highest rates of turbulent dissipation are associated with the warmest MWDW, with the vertical eddy diffusivity reaching $10^{-4}$ $m^2$ $s^{-1}$ where the water column is fully turbulent. Mixing efficiency is close to the canonical value of 0.2. Modeling studies suggest MWDW may become the dominant water mass beneath FRIS in our changing climate, providing strong motivation to understand more fully the dynamics of this MWDW inflow.

**Plain Language Summary** Filchner-Ronne Ice Shelf is the largest floating extension of the Antarctic Ice Sheet by volume. The ocean beneath it is cold and dense, and thus little ocean-driven melting occurs at its base. Climate models predict that a significant shift in ocean circulation within the sub-ice-shelf cavity may occur within the coming century, with large-scale inflows of warm water, highly elevated basal melt rates, and significant consequences for global sea level rise. Understanding the complex ice-ocean interactions that occur beneath Filchner-Ronne Ice Shelf is therefore critical. At present, only a single, narrow inflow of warm water is observed along Ronne Ice Front. The processes controlling this warm inflow are poorly understood, and here we present the first observations from the inflow region obtained using the unique autonomous Autosub Long Range underwater vehicle. We observe that the flow of warm water into the cavity extends at least 18 km and is highly patchy in nature, with isolated maxima in ocean temperature that are moved around by the tides. Vertical mixing is strongest where the ocean is warmest, contributing to diffusing and eroding the warm water signature. Many questions remain, motivating further studies with both autonomous and traditional observing platforms.

## 1. Introduction

Filchner-Ronne Ice Shelf (FRIS; Figure 1) located in the Weddell Sea sector of West Antarctica accounts for over 10% of all ice discharge from the Antarctic Ice Sheet (Gardner et al., 2018). By exerting considerable back stress on grounded ice upstream, it plays a role in regulating Antarctica's contribution to global sea level rise (Fürst et al., 2016; Reese et al., 2018). The water mass transformations that occur on the continental shelf and in the sub-ice-shelf cavity generate deep, cold and dense water masses that feed the lower limb of the global overturning circulation (Nicholls et al., 2009). Located to the south of the wide Weddell Sea continental shelf, which is dominated by cold and dense shelf waters, the cavity beneath FRIS is characterized by ocean temperatures that

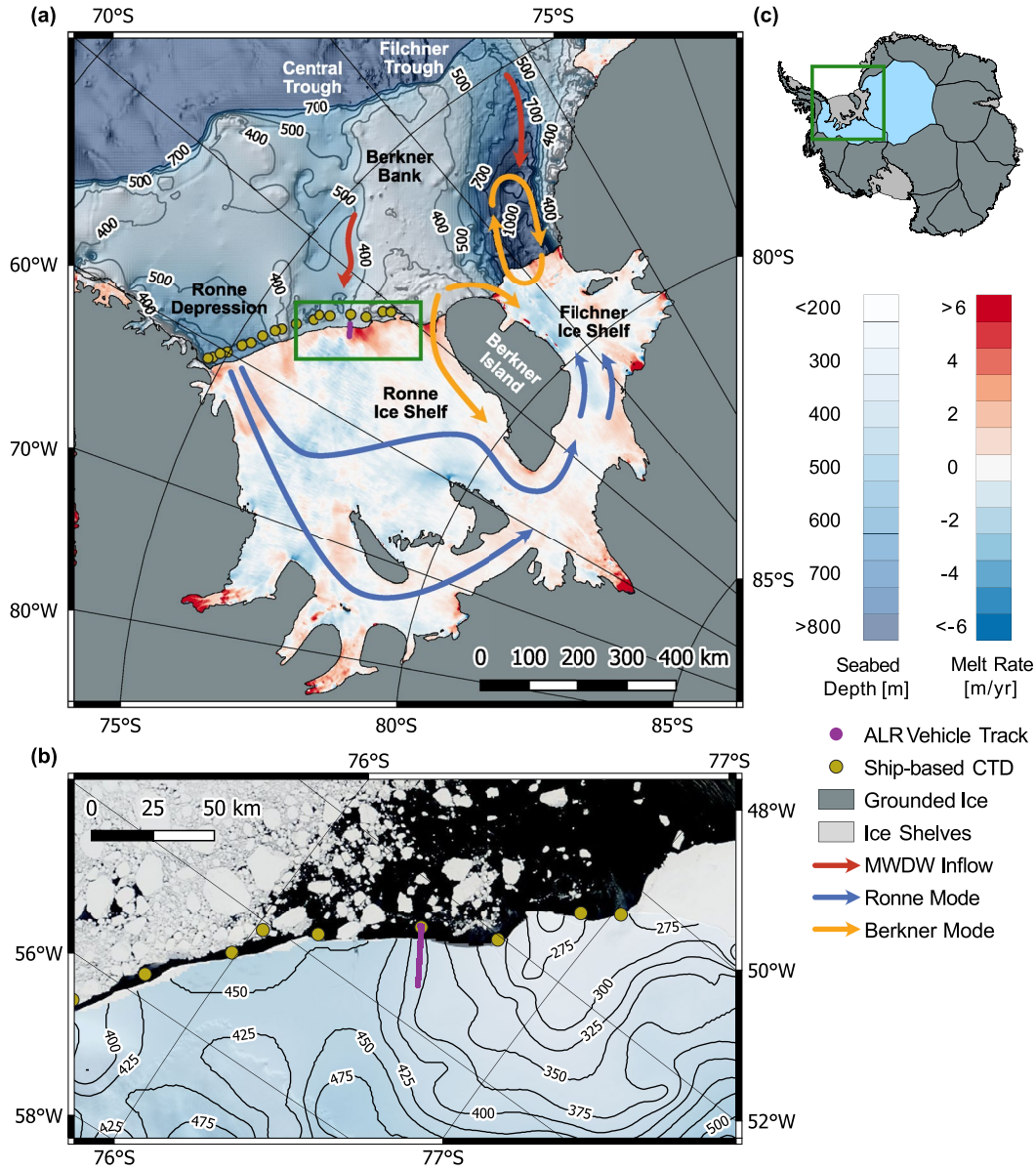


**Figure 1.** (a) Map of Filchner-Ronne Ice Shelf showing the Autosub Long Range AUV mission track. For ice shelf areas, colored contours (blue-red) show mean basal melt rates between 2010 and 2018 derived from Cyrosat-2 altimetry data (Adusumilli et al., 2020). For open water areas, colored contours (blue-white) show seabed depth from the International Bathymetric Chart of the Southern Ocean (Arndt et al., 2013) with contour lines every 100 m over the continental shelf. Colored arrows show the main circulation regimes and inflow pathways of MWDW. Yellow dots along the Ronne Ice Shelf Front show the location of ship-based CTD stations (Janout et al., 2021). (b) Moderate Resolution Imaging Spectroradiometer (MODIS) satellite image from 8th February 2018 of Ronne Ice Front (green box in main panel) overlaid with the AUV mission track and sub-ice-shelf seabed depth from Bedmap2 (Fretwell et al., 2013). Bedmap2 bed depth has been shifted 20 m shallower to align with the observed bed depth from Autosub Long Range (see Section 2.2). (c) Overview of Antarctica with the location of the area covered in (a) shown by the green box. Thin black lines delineate the major ice sheet drainage basins, with the Filchner-Ronne drainage basin highlighted in light blue.

are at or below the surface freezing point (<−1.9°C; Nicholls et al., 2009). Average basal melt rates beneath FRIS are therefore low (0.35 m $yr^{-1}$; Timmermann et al., 2012) with some areas of refreezing (Adusumilli et al., 2020, Figure 1a), and the overall volume of ice lost due to basal melting is relatively small for its areal extent (Rignot et al., 2013). This stands in contrast to the "warm cavity" ice shelves (Jenkins et al., 2016; Thompson et al., 2018) found in the Amundsen Sea sector of West Antarctica, where strong ocean forcing driven by warm waters (+1.0°C)

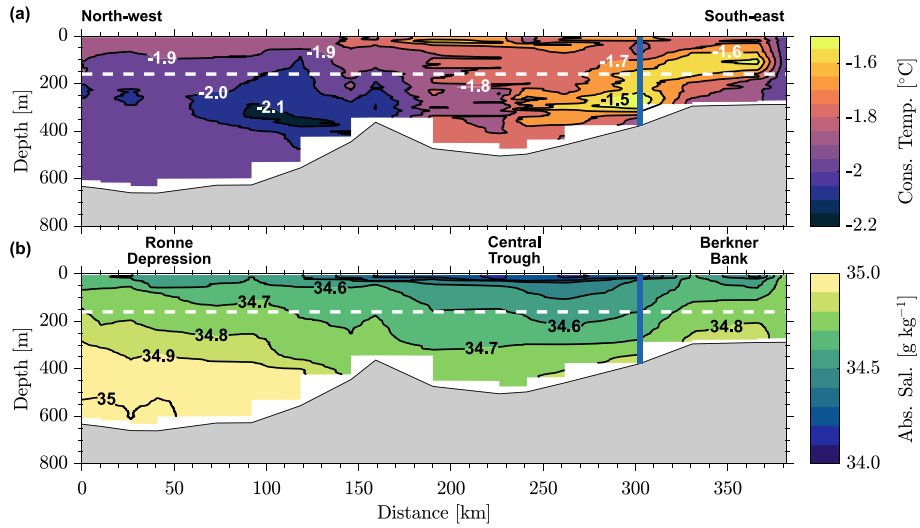


**Figure 2.** Sections of (a) Conservative Temperature and (b) Absolute Salinity along the Ronne Ice Front (yellow dots in Figure 1a and 1b) in austral summer 2018 from the RV *Polarstern* PS111-expedition to the southern Weddell Sea (Janout et al., 2021). Sections are plotted as a function of distance from the western-most PS111 station. The blue line at ∼300 km marks the location where ALR entered the Ronne Ice Shelf cavity, following the warm core of MWDW that hugs the eastern flank of the Central Trough (see Figure 1a). The dashed white line shows the ice shelf draft at the location of the ALR mission.

that originate north of the continental shelf (Hellmer et al., 1998; Jacobs et al., 1996; Wåhlin et al., 2010) is driving rapidly increasing rates of basal melting and ice shelf volume loss (IMBIE, 2018; Paolo et al., 2015).

Exchange of water masses across Filchner-Ronne Ice Front is thought to be controlled by the density gradient that exists between the salty and dense water masses found on the Weddell Sea continental shelf, and the lighter and fresher waters found within the FRIS cavity (Nicholls et al., 2009). This exchange is modulated by the potential vorticity barrier present at the ice front (Darelius et al., 2014). Strong sea ice production, export, and brine rejection over the continental shelf and within coastal polynyas along Ronne Ice Front (Haid & Timmermann, 2013; Hattermann et al., 2021) form a cold and dense water mass known as High Salinity Shelf Water (HSSW) that is cooled to the surface freezing point (−1.9°C; Nicholls et al., 2009). The densest form of HSSW flows into the FRIS cavity following the bathymetry of the Ronne Depression (Nicholls et al., 2001, 2004; Timmermann et al., 2012, Figure 1a), while a less saline form of HSSW flows into the cavity along the western coast of Berkner Island (Foldvik et al., 2001, Figures 1a and 2). As HSSW travels through the cavity it drives basal melting due to the pressure dependence of the freezing point (Lewis & Perkin, 1986), creating a colder, fresher, and slightly lighter water mass known as Ice Shelf Water (ISW; Gade, 1979). ISW is supercooled relative to the surface freezing point and flows out of the cavity via the Filchner Trough (Darelius & Sallée, 2018; Janout et al., 2021; Nicholls et al., 2009). On interannual timescales, the FRIS cavity exhibits two modes of circulation (the Ronne-mode or Berkner-mode) depending on the dominant HSSW source, driven by changes in atmospheric circulation and sea ice production in the southwestern Weddell Sea (Figure 1a; Hattermann et al., 2021; Janout et al., 2021). A recent transition to the Ronne-mode fostered a stronger inflow of HSSW via the Ronne Depression that increased the input of heat into the sub-ice-shelf cavity available to drive basal melting and enhanced the outflow of ISW through the Filchner Trough (Janout et al., 2021).

The cold and dense water masses found on the shelf and beneath FRIS prevent any large-scale and widespread inflow of the Circumpolar-Deep-Water-derived Warm Deep Water (WDW) that circulates offshore of the Weddell Sea continental shelf (Vernet et al., 2019) into the ice shelf cavity. However, there are two locations where persistent intrusions of WDW-derived water masses have been observed on the continental shelf. In the Filchner Trough, seasonal inflows of Modified Warm Deep Water (MWDW) are able to penetrate as far south as the Filchner Ice Front (Årthun et al., 2012; Darelius & Nicholls, 2016; Foldvik et al., 1985; Ryan et al., 2020, Figure 1a) after WDW mixes with colder and fresher Eastern Shelf Waters off Dronning Maud Land and Coats Land (Carmack, 1974; Hattermann, 2018; Ryan et al., 2017; Stewart & Thompson, 2015). However, as this MWDW is found above the denser HSSW and ISW that occupy the deepest parts of the Filchner Trough

**Table 1**
*Table of Symbols and Their Definitions Used Throughout This Study*

| Symbol | Definition |
|---|---|
| $\Theta$ | Conservative temperature |
| $S_A$ | Absolute salinity |
| $f$ | Frequency |
| $k$ | Wavenumber |
| $\nu$ | Kinematic viscosity of seawater |
| $\partial u'/\partial z$ | Vertical velocity shear fluctuations |
| $\psi_S(f)$ | Velocity shear frequency spectrum |
| $\psi_S(k)$ | Velocity shear wavenumber spectrum |
| $W$ | Relative flow speed past the shear probes/thermistors |
| $H_s(k)$ | Single-pole transfer function for shear probes |
| $\chi$ | Thermal variance dissipation |
| $\kappa_T$ | Molecular thermal diffusivity |
| $\partial T'/\partial z$ | Vertical temperature gradient fluctuations |
| $\psi_T(k)$ | Temperature gradient wavenumber spectrum |
| $H_T(f)$ | Double-pole transfer function for thermistor probes |
| $\tau$ | Thermistor response time constant |
| $k_b$ | Batchelor wavenumber |
| $K_\rho$ | Vertical eddy diffusivity |
| $\overline{N}$ | Background buoyancy frequency |
| $\Gamma$ | Mixing efficiency |
| $Ri_f$ | Flux Richardson number |
| $\partial\overline{T}/\partial z$ | Background vertical temperature gradient |
| $Q_T$ | Vertical heat flux |
| $\rho$ | Density of seawater |
| $C_p$ | Specific heat capacity of seawater |
| $R_\epsilon$ | Buoyancy Reynolds number |
| $\rho_i$ | Density of ice |
| $L_i$ | Latent heat of fusion of ice |
| $\dot{m}$ | Basal melt rate |
| $K_i$ | Thermal conductivity of ice |
| $c_i$ | Specific heat capacity of ice |
| $\kappa_i^T$ | Thermal diffusivity of ice |
| $\partial T_i/\partial z$ | Ice base temperature gradient |

(Janout et al., 2021), it resides at depths shallower than the ice front draft (~450 m) and does not contribute significantly to basal melting. While some modeling studies have indicated that freshening shelf waters under warmer atmospheric conditions may erode the density barrier and lead to enhanced inflow of MWDW through Filchner Trough and a significant increase in FRIS basal melting by the end of this century (Daae et al., 2020; Hellmer et al., 2012, 2017), other studies suggest that this may only occur under the most extreme climate forcing scenarios (Naughten et al., 2021).

A second inflow of MWDW is observed at the Ronne Ice Front along the west side of Berkner Bank (draft ~160 m; Foldvik et al., 2001; Gammelsrød & Slotsvik, 1981). This core of MWDW is guided south-westward through the Central Trough of the Weddell Sea continental shelf (Figure 1a), arriving at the ice front with a maximum temperature of up to −1.1°C (Foldvik et al., 2001; Janout et al., 2021, Figure 2). This is considerably cooler than its temperature at the shelf break (−0.2°C), indicating that it loses a significant amount of heat during its ~500 km passage across the continental shelf. The inflow, which reaches the ice front at a depth of ~350 m (Figure 2) and has a geostrophic velocity core of ~5 cm $s^{-1}$ (Janout et al., 2021), appears to drive strong basal melting near the ice front (Adusumilli et al., 2020). The region of elevated basal melting, however, is small compared with the total area of the ice shelf (Figure 1a), indicating that the influence of MWDW beneath Ronne Ice Shelf is geographically limited. While the presence of MWDW at Ronne Ice Front has been known for some time (e.g., Gammelsrød & Slotsvik, 1981), the dynamics governing its inflow, its ultimate fate, and its effect on basal melting beneath Ronne Ice Shelf remain largely unknown. Here we present the first hydrographic, velocity and microstructure measurements taken along the MWDW inflow beneath Ronne Ice Shelf using the Autosub Long Range autonomous underwater vehicle (AUV). AUV technology allows data to be gathered beneath ice shelves at much higher spatial resolution than that available from traditional sub-ice shelf moorings, thus enabling us to investigate in unprecedented detail the evolution of the MWDW properties as it transits the ice front. We begin with a description of the ALR sub-ice-shelf mission and the methods used to process the velocity, hydrographic and microstructure data in Section 2. In Section 3 we present the results along the vehicle's track as a function of distance from the ice front, describing the water column hydrographic structure and velocity field, as well as the rate and distribution of turbulent kinetic energy dissipation, the mixing efficiency, and the vertical heat flux. Implications and conclusions are discussed in Section 4. A summary of symbols used throughout this study is given in Table 1.

## 2. Autosub Long Range Observations and Methods

### 2.1. Sub-Ice-Shelf Mission Overview

Autosub Long Range (ALR) was deployed for a single mission beneath Ronne Ice Shelf following the inflow pathway of MWDW from the German research icebreaker RV *Polarstern* (AWI, 2017) during the PS111-expedition to the southern Weddell Sea (Figure 1b; Janout et al., 2021; Schröder, 2018). The mission track ran along the core of MWDW that hugs the eastern flank of the Central Trough (Figure 2), from a point 5 km north-east of the ice front to a point 20 km beneath the ice. ALR followed a great-circle course approximately parallel to the 400 m isobath, alternating between stretches of bottom tracking and top tracking in a square-wave pattern, while maintaining a minimum clearance of 80 m between the vehicle and the ice base or seabed. This mission plan was designed to minimize vehicle pitching in order to maximize the accuracy of the vehicle's dead-reckoning navigation system, which

makes use of ALR's bottom and top track DVL data that cannot be updated with GPS fixes under the ice, while also providing periodic water column profiles. When ALR is pitching, the DVLs have less chance to get top/bottom lock due to the increased range and angle of incidence of the acoustic beams when they are tilted away from the reference surface, degrading the quality of the navigation data as well as the velocity and turbulence data. ALR's control system was programmed to maintain the set altitude of 80 m over a variety of seabed and ice base topographies, however strict pitch limits were also imposed (+40° to −20°) to maintain the quality of the sensor data. Ultimately these limits were never reached, and the pitch angle was no greater than ±17° during the climbing and diving phases. The steady state pitch angle was generally less than ±2°.

ALR was deployed on 9 February 2018, at 14:25 UTC, and was recovered approximately 25.6 hours later on 10 February 2018, at 16:04 UTC. The timing of the mission was planned to coincide with neap tides, to minimize the effect of strong across-track currents on the vehicle. In total, ALR spent 13.9 hours beneath Ronne Ice Shelf, traveling at an average speed of 0.7 ± 0.1 m $s^{-1}$ and reaching a maximum distance of 18.2 km from the ice front. An iXblue Ultra-Short Baseline Global Acoustic Positioning System (GAPS-USBL) was used to track ALR at the point of deployment, when it first entered the ice shelf cavity and when the vehicle was recovered, allowing the heading (−0.86°) and speed (0.9884) errors to be quantified. These data were used to calibrate the vehicle's real-time dead-reckoning navigation post-mission. ALR was equipped with a Seabird SBE-52 Conductivity-Temperature-Depth (CTD) sensor, two Teledyne RDI 300 kHz Workhorse Acoustic Doppler Current Profilers (ADCPs), one upward looking and one downward looking, and a nose-mounted Rockland Scientific International (RSI) MicroRider turbulence package. Additional information is available in the PS111 cruise report (Schröder, 2018).

### 2.2. ADCP Velocity Data

Both upward and downward looking RDI 300 kHz Workhorse ADCPs were configured in bottom track mode with 8 m bins and used for navigation as well as current measurements. Each ADCP was set to ping once every 2 seconds, with half-second ping separation between instruments to avoid interference, and the raw velocity data were processed using 5-ping (10 second) averaging. Current velocities in the vehicle frame were calculated by subtracting the bottom track velocity from the raw upwards and downwards-looking water track velocities and were then rotated into a geographic reference frame using the vehicle's heading. Geographic velocities were then cast into the along- and across-track direction using the mean mission track heading (56.5° east of geographic north). As ALR was programmed to run a constant course (Figure 1b), the along-track velocity is largely defined as the flow parallel to the direction of vehicle travel (defined as positive out of the cavity), while the across-track velocity is defined as the flow perpendicular to the direction of vehicle travel (defined as positive toward the south-east). Following the approach detailed in Naveira Garabato and Forryan (2017), erroneous velocities (large amplitude and large variance) for both the upward and downward looking ADCPs were identified and masked in the bin nearest to the vehicle, as well as in all bins with a range greater than 66 m. Further quality control of the ADCP data was carried out using the ADCP beam echo intensity and percent good diagnostic fields. Velocity data were flagged as erroneous when the percentage of measurements where more than one beam was bad exceeded 80%, or the percentage of measurements with four beam solutions was less than 20%, or the beam echo intensity exceeded 180 (which is caused by reflections from the seabed or ice base). Despite the quantitative quality control, some small artifacts remain in the ADCP data, however these do not affect the conclusions of this study.

A variety of approaches were used to determine the magnitude of the tidal current along ALR's track for the four major tidal constituents (M2, S2, O1 and K1), including least-squares harmonic analysis (Pawlowicz et al., 2002) and extracting tidal components from the 2008 Circum-Antarctic Tidal Simulation, which is an update to the model described in Padman et al. (2002). While the model-based approaches demonstrated that tidal variability is dominant (Figure S1 in the Supporting Information S1), the best fit (i.e., the fit which minimizes residual velocities at tidal frequencies in the detided ADCP data; Figure S2 in the Supporting Information S1) was achieved through spatially-invariant harmonic analysis of the depth-averaged ADCP velocities (Figure S1 in the Supporting Information S1). More sophisticated fits using spatially varying harmonic analysis, which combines the classical least-squares fitting technique with second-order polynomials to empirically model the spatial variation in phase and amplitude of the tidal components as a function of latitude and longitude (Allen, 1995), did

not significantly improve the tidal fit (Figure S1 in the Supporting Information S1), and therefore we took the simplest approach of assuming the tidal components were constant along ALR's track.

When in range, the upward and downward looking ADCPs observed the distance to the ice base and seabed along the vehicle track. Comparing observed bed depth and ice draft with co-located estimates from Bedmap2 (Fretwell et al., 2013) showed that the ice draft along the vehicle track is 52 m shallower than that in Bedmap2, while the sea bed is 20 m shallower. Consequently, Bedmap2 bed depth and ice draft data have been shifted vertically throughout this paper to align with the observed bathymetry from ALR. Furthermore, from contemporaneous WorldView satellite imagery the Ronne Ice Front in February 2018 (Figure 1b) was observed to be 20 km further north than its position in Bedmap2, and thus the Bedmap2 ice draft data were also shifted horizontally to align with the 2018 ice front position.

### 2.3. Hydrographic Data

ALR was equipped with a Seabird SBE-52 CTD that contains a ducted, pumped conductivity-temperature channel and samples at a rate of 1 Hz. The stated accuracy is ±0.002°C for temperature and ±0.003 mS cm$^{-1}$ for conductivity. The SBE-52 was mounted toward the front of the vehicle with the inlet and exhaust ducts attached to a pair of ports in the vehicle's hull. Post-deployment, the SBE-52 was compared against the post-cruise calibrated ship-based CTD data taken from RV *Polarstern*, and small corrections were made to both the temperature (+0.0024°C) and conductivity (+0.0022 mS cm$^{-1}$) recorded by ALR. Absolute Salinity ($S_A$) and Conservative Temperature ($\Theta$) were derived using the standard 2010 Thermodynamic Equation of State (McDougall & Barker, 2011).

### 2.4. Microstructure Data

The RSI MicroRider package had four microstructure probes sampling at a rate of 512 Hz: two orthogonally positioned shear probes that provide an estimate of the rate of turbulent kinetic energy dissipation (TKE; $\varepsilon$), and two thermistor probes that provide an estimate of the rate of thermal variance dissipation ($\chi$). The microstructure data were processed following standard methods (e.g., Inall et al., 2022; Kimura et al., 2016; Piccolroaz et al., 2021; Scott et al., 2021). Under the assumption of small-scale isotropy, $\varepsilon$ can be estimated as

$$\varepsilon = \frac{15}{2}\nu\left\langle\left(\frac{\partial u'}{\partial z}\right)^2\right\rangle = \frac{15}{2}\nu\int_0^{k_I}\psi_S(k)\,dk, \tag{1}$$

where $\nu$ is the temperature-dependant kinematic viscosity of seawater and $\left\langle\left(\partial u'/\partial z\right)^2\right\rangle$ is the variance of the velocity shear fluctuations perpendicular to ALR's path (Osborn, 1974) derived from integrating the velocity shear spectrum $\psi_S$ in wavenumber space $k$ up to $k_I$. Converting the raw data from the shear probes into physical units requires knowledge of the relative flow speed past the sensors. The relative flow speed is derived from the ADCP water and bottom track velocities and is corrected for the changing pitch of the vehicle. With pitch angles <17°, this correction is no greater than 5% (Naveira Garabato & Forryan, 2017). Initially, shear spectra in frequency space $\psi_S(f)$ were calculated for each 2 second segment of data, with a 50% overlap between segments, and then averaged in half-overlapping 20 second windows to increase the signal-to-noise ratio. With an average vehicle speed of ~0.7 m s$^{-1}$, this approach provides 5656 half-overlapped estimates of $\varepsilon$ every 7.5 m. For each 20-second segment, the mean relative flow speed past the shear/thermistor probes $W$ was used to convert frequency to wavenumber using Taylor's frozen turbulence hypothesis (Bluteau et al., 2016).

$$\psi_S(k) = W\psi_S(f) \text{ and } k = fW^{-1} \tag{2}$$

The raw shear signals are contaminated by vehicle vibrations (especially in low energy regions of the cavity), which appear as a spurious peak in the shear spectra at a frequency of ~5–10 Hz. These peaks were removed by constructing a coherent noise removal filter using accelerometer signals from the RSI MicroRider (Figure S3 in the Supporting Information S1; Levine & Lueck, 1999). Each shear spectrum was corrected for the shear probe's spatial response by dividing by a single pole transfer function $H(k)$ (Bluteau et al., 2016; Macoun & Lueck, 2004; Piccolroaz et al., 2021).

$$H_s(k) = \frac{1}{1 + (k/k_c)^2}, \tag{3}$$

where the half-power wavenumber $k_c = 48$ cycles per meter (cpm) for Rockland Scientific's shear probes. The integration limit $k_I$ in Equation 1 was selected such that it resolved a sufficient portion of the shear variance over the inertial subrange, while minimizing contributions from the noise-dominated portions of the spectra found at higher wavenumbers. For each shear spectrum, $k_I$was set to at least 10 cpm, or if larger, the minimum of (1) the wavenumber that resolves 95% of the shear variance $k_{95}$, (2) the global spectral minimum, which indicates the highest wavenumber before noise dominates the spectra, or (3) 150 cpm where $H_s(k)$ results in a correction factor that exceeds an order of magnitude (Bluteau et al., 2016). For the relatively low rates of dissipation found beneath Ronne Ice Shelf ($\varepsilon < 10^{-9}$ W m$^{-2}$), integrating up to 10 cpm resolved a sufficient portion of the shear variance in 58.1% of spectra, while integrating to $k_{95}$ was sufficient in a further 41.7% of cases. Each estimate of $\varepsilon$ was then iteratively adjusted using the empirical Nasmyth spectrum to correct for the shear variance found beyond $k_I$ and at the low-wavenumber end of the spectrum (Lueck, 2016; Piccolroaz et al., 2021). Turbulence has a correlation time and length scale, and therefore 88 $\varepsilon$ estimates that differed by more than a factor of 4 between shear probes for the same segment, or more than a factor of 10 between neighboring segments, were discarded.

In conjunction with $\varepsilon$, the rate of thermal variance dissipation $\chi$ was calculated assuming small-scale isotropy

$$\chi = 6\kappa_T \left\langle \left( \frac{\partial T'}{\partial z} \right)^2 \right\rangle = 6\kappa_T \int_0^{k_I} \psi_T(k)\, dk, \tag{4}$$

where $\kappa_T$ is the molecular thermal diffusivity and $\left\langle \left(\partial T'/\partial z\right)^2 \right\rangle$ is the temperature gradient variance, estimated by integrating the temperature gradient wavenumber spectrum $\psi_T(k)$ up to $k_I$. Each temperature gradient spectrum was corrected for the thermistor's frequency response using a double-pole transfer function

$$H_T(f) = \left[1 + (2\pi\tau f)^2\right]^{-2}, \tag{5}$$

where the time constant $\tau = \tau_0 \left(\overline{W}/W_0\right)^{-0.5}$, $\tau_0 = 4.1 \times 10^{-3}$ s and $W_0 = 1.0$ m s$^{-1}$ (Vachon & Lueck, 1984). $k_I$ was set to $0.3k_b$ (where $k_b = \left[\varepsilon/\left(\nu\kappa_T^2\right)\right]^{1/4}$ rad m$^{-1}$ is the Batchelor wavenumber) at which almost 50% of the temperature gradient variance contributing to $\chi$ is resolved (Bluteau et al., 2017), and a correction factor was used to account for the variance at unresolved wavenumbers following the approach of Peters et al. (1988). For 22 segments, the frequency correction factor $H_T(f)$ at $0.3k_b$ was >5 (Bluteau et al., 2017), or the ratio between the observed temperature gradient spectrum and the underlying noise spectrum was <1.5 (Peterson & Fer, 2014), and therefore the estimate of $\chi$ was discarded. A further 98 $\chi$ values that differed by more than a factor of 4 between thermistors, or by more than a factor of 10 from neighboring values were also discarded.

Using data from sections of the mission track where ALR was profiling the water column, the vertical eddy diffusivity was calculated using the Osborn model (Osborn, 1980).

$$K_\rho = \Gamma \frac{\varepsilon}{\overline{N}^2}, \tag{6}$$

where $\Gamma = Ri_f/(1 - Ri_f)$ is the mixing efficiency (a measure of the amount of turbulent kinetic energy that is irreversibly converted to background potential energy due to turbulent mixing), $Ri_f$ is the flux Richardson number and $\overline{N}$ is the background buoyancy frequency calculated from sorted vertical density profiles. In geophysical settings, $\Gamma$ is canonically set to a value of 0.2 ($Ri_f = 0.17$; Shih et al., 2005), however it is known to vary widely (e.g., Bluteau et al., 2013; Salehipour et al., 2015). Instead, $\Gamma$ can be calculated directly by equating the Osborn–Cox model for the vertical diffusivity of heat (Osborn & Cox, 1972).

$$K_T = \frac{1}{2} \frac{\chi}{\left(\frac{\partial \overline{T}}{\partial z}\right)^2}, \tag{7}$$

where $\partial\overline{T}/\partial z$ is the background vertical temperature gradient, to the Osborn model for the vertical eddy diffusivity (Equation 6):

$$\Gamma = \frac{\overline{N}^2}{2\left(\frac{\partial\overline{T}}{\partial z}\right)^2}\frac{\chi}{\varepsilon}. \tag{8}$$

Using $K_\rho$, vertical heat fluxes were estimated from

$$Q_T = \rho C_p K_\rho \frac{\partial\overline{T}}{\partial z}, \tag{9}$$

where $\rho$ is density and $C_p = 3974$ J kg$^{-1}$ °C$^{-1}$ is the specific heat capacity of seawater.

## 3. Results

Here we present the hydrographic structure, ADCP velocity data and microstructure observations along the MWDW inflow beneath Ronne Ice Shelf. We begin with the velocity field, which is central to setting the spatial/temporal variability in the turbulence and hydrographic properties.

### 3.1. Velocity

Consistent with previous models and observations (Foldvik et al., 2001; Makinson & Nicholls, 1999), current velocities along the MWDW inflow are dominated by tidal variability. The maximum current speed observed by ALR reached 29 cm s$^{-1}$, which coincided with the period of strongest tidal flow ~15–17 km from the Ronne Ice Front on the return leg (Figure 3). Spatial variability in the current velocity is predominantly associated with temporal variability in the tidal flow. At the beginning of ALR's mission, the tidal current is flowing at maximum velocity into the cavity (negative values, Figures 3a and 3c), with a general across-track flow to the south-east (Figure 3b). At ~8.6 km distance from the ice front, or ~5 hours into the mission, the tidal current reverses direction and begins to flow out of the cavity with an across track component to the north-west. Observed tidal variability is in general agreement with that predicted by barotropic tidal models (Padman et al., 2002), however, phase and amplitude differences are observed (Figure S1 in the Supporting Information S1). Initially running against this reversed current, ALR reaches its turning point 18 km from the ice front and then begins to run with the tide for a further 7 hours before the tidal current reverses again as ALR passes out of the cavity. The tidal flow is largely barotropic, although there is some limited evidence of phase change with depth when the tidal current is reversing direction (Makinson et al., 2006, Figure 3). The combined tidal current ellipse is oriented at an angle to ALR's track, lying geographically in a north to south direction (Figure 4a). During the period of ALR's mission that the along-track tidal current is directed out of the ice shelf cavity, the net tidal advection is ~5.6 km toward the ice front. This tidal advection and the temporal variability in the tidal current direction is largely responsible for setting the sub-ice-shelf spatial variability in hydrographic and turbulent parameters.

At the depth of the core MWDW inflow (250–350 m; Figure 2), the detided current observed by ALR is directed into the cavity throughout the mission, with a mean along-track velocity of $-4.0 \pm 1.6$ cm s$^{-1}$ (Figure 5a). This is consistent with the baroclinic-only geostrophic velocity estimate of the MWDW inflow derived from ship-based CTD stations at the ice shelf front (Janout et al., 2021). The detided across-track component at this depth is small (<1 cm s$^{-1}$; Figure 4b), consistent with a topographically controlled inflow that follows isobaths. Ignoring the advective effect of the tides (which is highly asymmetrical due to the short observation period of ALR's mission), the strength of the detided flow results in a ~2.5 km south-westward advection of MWDW into the ice shelf cavity (Figure 4b). Above the depth of the MWDW inflow, at a distance of ~5 km from the ice front on both the outbound and return legs, there is a consistent detided across-track flow to the south-east with mean velocity of 4.8 cm s$^{-1}$ (Figure 5b). South-eastward flow aligned parallel to the ice front is consistent with an along-track density gradient (Section 3.2), or steering of barotropic flow by the topographic step associated with the ice shelf front (Darelius et al., 2014; Wåhlin et al., 2020). This flow feature is discussed in more detail later (Section 4).

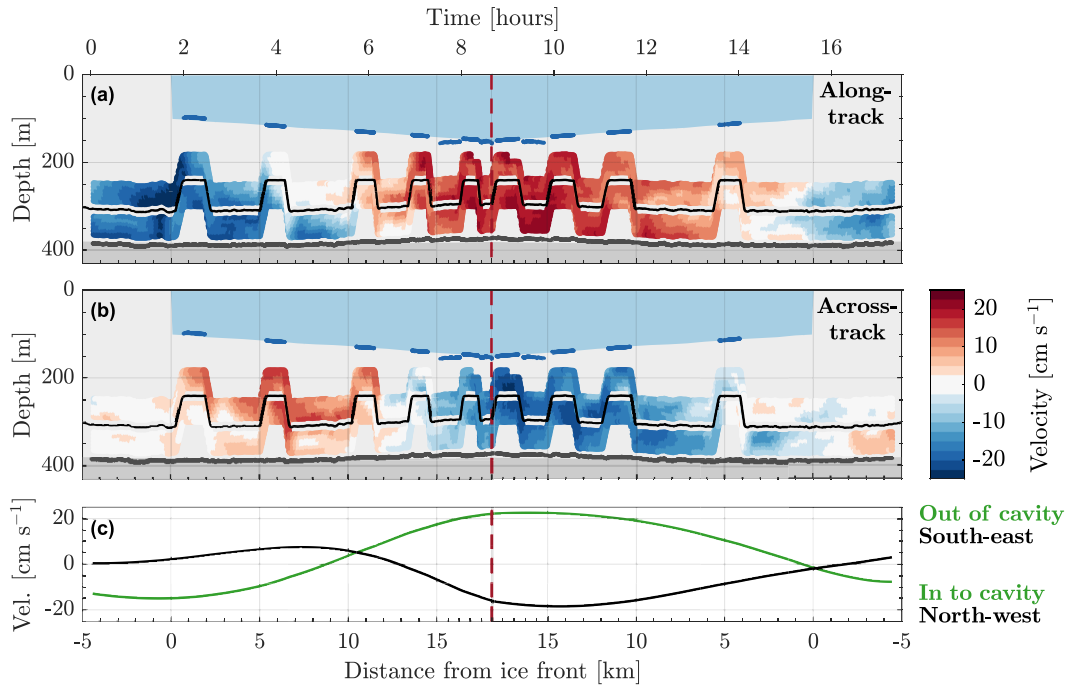


**Figure 3.** Water column velocities observed by the upward- and downward-looking ADCPs in (a) the along-track and (b) the across-track direction. The data are plotted as a function of depth and distance from the ice front. The left-hand portion of each panel shows the outbound leg of ALR's mission up to the turning point (red dashed line) at ~18 km from the ice front. The right-hand portion of each panel shows the return leg. The solid black line shows the depth of ALR as it transits through the cavity. The broken blue line above ALR's track shows the observed depth of the ice shelf base when it was in range, while the light blue patch shows the horizontally and vertically adjusted ice base from Bedmap2. The gray dots below ALR's track show the observed depth of the seabed, with the vertically adjusted Bedmap2 seabed shown by the light gray patch. Positive velocities are directed out of the cavity or across ALR's track in a south-eastward direction, while negative velocities are directed into the cavity or across ALR's track in a north-westward direction. (c) along-track (green) and across-track (black) tidal velocities derived through harmonic analysis.

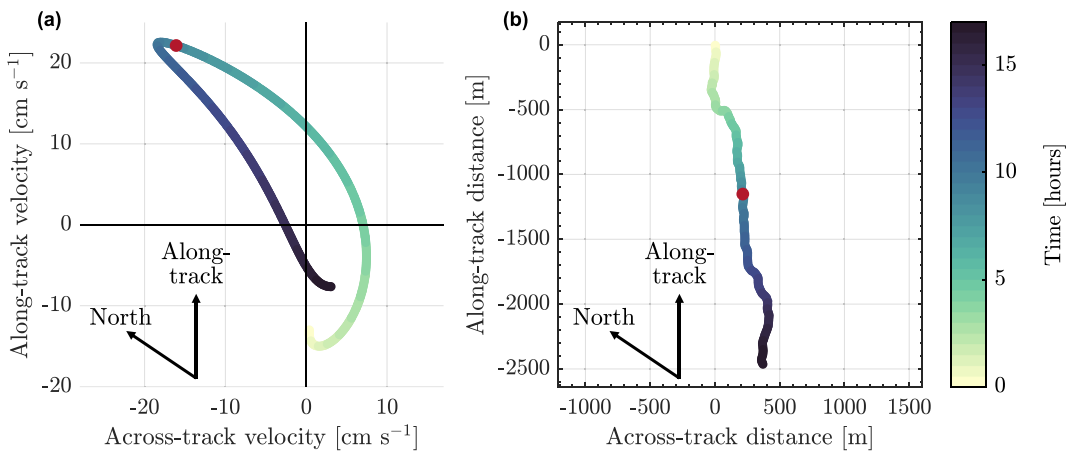


**Figure 4.** (a) Combined tidal current ellipse in an along/across-track frame of reference for the four major tidal constituents plotted as a function of time. The along-track and across-track velocity series are those presented in Figure 3c. (b) progressive vector diagram for the detided flow averaged over the depth of the MWDW inflow (250–350 m) for the duration of ALR's mission, plotted as a function of time. The red dots in (a) and (b) mark the turn-around point of ALR's mission.

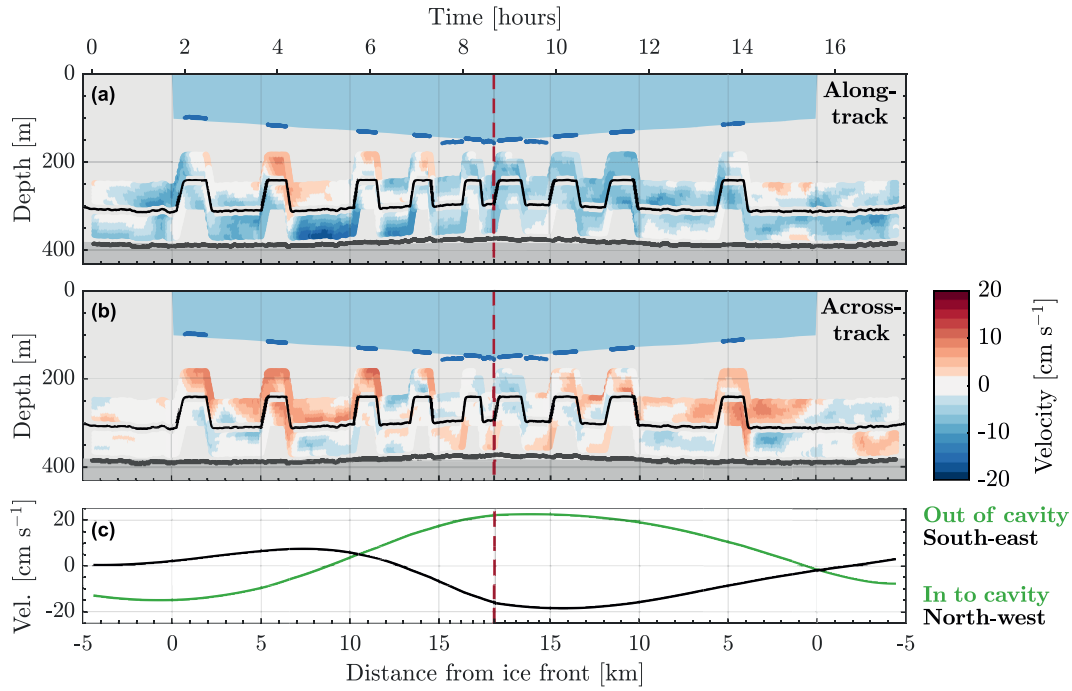


**Figure 5.** Detided water column velocities plotted in the same format as Figure 3 for (a) the along-track direction and (b) the across-track direction. Note the different color scale compared to Figure 3. (c) along-track (green) and across-track (black) tidal velocities derived through harmonic analysis.

### 3.2. Hydrography

The hydrographic properties along ALR's track (Figure 6) largely consist of three separate water masses: cold and fresh surface waters ($S_A < 34.67$ g kg$^{-1}$ and $\Theta < -1.6$°C), warm MWDW ($\Theta > -1.5$°C), and cold and salty HSSW ($S_A > 34.75$ g kg$^{-1}$ and $\Theta < -1.6$°C; Figure 7). The water column is above the surface freezing point everywhere, but there is no clear evidence of glacial melt water, which would appear in $\Theta$-$S_A$ space along a straight meltwater mixing line with a slope of $\sim 2.65\ \Theta\ S_A^{-1}$ (McDougall et al., 2014). Instead, $\Theta$-$S_A$ data from ALR evolve along a steeper trajectory (Figure 7a), indicating that basal melting is not driving the observed variation in $\Theta$ and $S_A$. This behavior is consistent with the relatively large vertical distance between ALR's track and the ice base, where basal melting is very likely to be occurring, and the limited time available for meltwater to be mixed through the water column given the proximity of ALR's mission to the ice front. The water column is salt-stratified (Figures 6b and 6c), with the freshest surface waters ($\sigma_T < 27.8$ kg m$^{-3}$) lying above denser MWDW and the densest HSSW ($\sigma_T > 27.85$ kg m$^{-3}$). Outside of the cavity, this stratification is not present year-round, with observations showing that it is gradually eroded during late austral winter and spring due to sea ice production driving active convection (Foldvik et al., 2001). For all but three vertical profiles observed by ALR (marked with black dots in Figure 6a), the water column is doubly stable ($\Theta$ decreases with depth) and thus double diffusive effects are negligible. The densest HSSW observed by ALR has a maximum salinity of ~34.8 g kg$^{-1}$, and likely originates from Berkner Bank (Figure 7a, Akhoudas et al., 2020; Janout et al., 2021). The maximum salinity is ~0.02 g kg$^{-1}$ less than that observed at a depth of 285 m from full-depth ship-based CTD profiles over Berkner Bank (Figure 7a; Janout et al., 2019), and suggests that the saltiest HSSW cascades down the eastern flank of the Central Trough to settle beneath the maximum depth of ALR's track (300 m). A distinct patch of warm MWDW is observed ~11 km from the ice front on ALR's outbound leg and ~5 km from the ice front on the return leg (Figure 6a). The MWDW in this patch is warmer (maximum temperature −1.35°C) than any MWDW observed with contemporaneous ship-based data outside of the ice shelf cavity from PS111 (maximum temperature −1.40°C; Figure 7a), indicating that the inflow of the warmest MWDW beneath Ronne Ice Shelf might be highly sporadic (Foldvik et al., 2001). Thermal driving, the difference between the in-situ temperature and the in-situ freezing point at the depth of the ice base, reaches 0.63°C, indicating that the MWDW inflow brings a significant amount of heat into the Ronne Ice Shelf cavity that is available to drive basal melting.

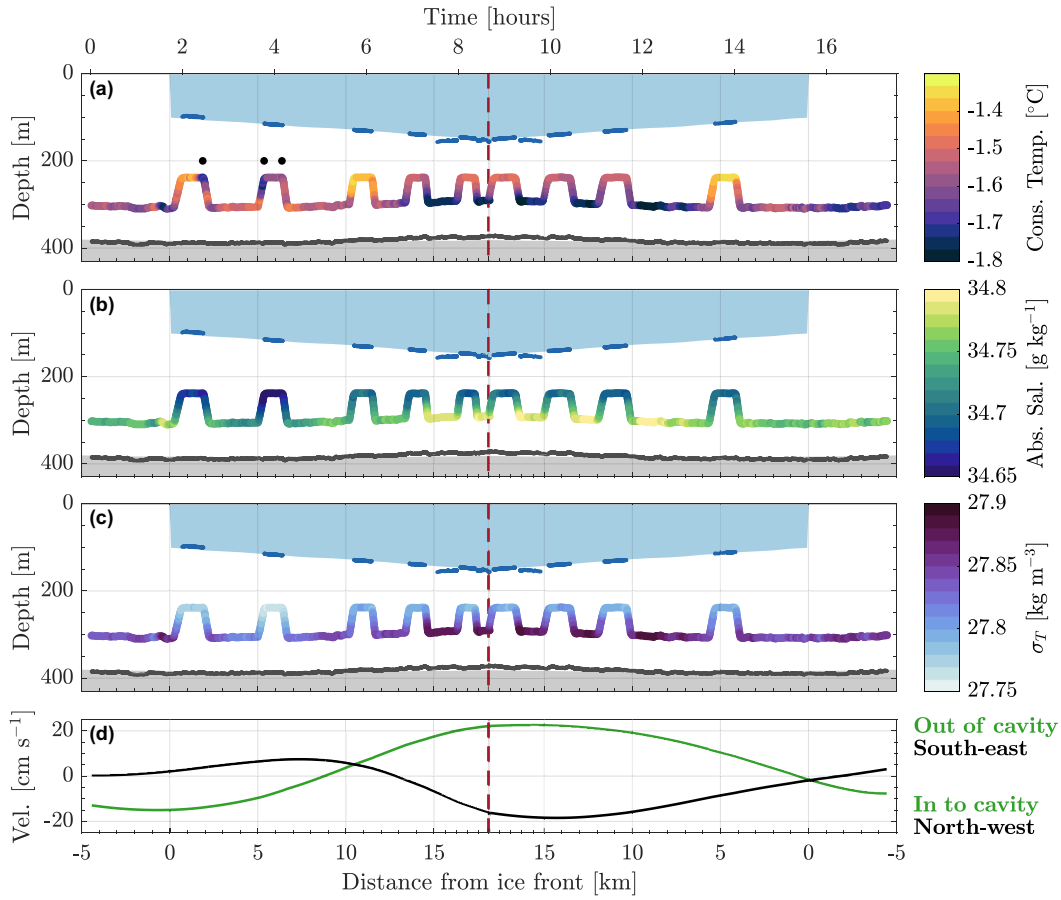


**Figure 6.** (a) Conservative Temperature, (b) Absolute Salinity, and (c) sigma-t referenced to the sea surface along ALR's track plotted in the same format as Figure 3. The black dots in panel (a) mark the water column profiles where Θ does not decrease with depth and therefore the water column is susceptible to diffusive convection. (d) along-track (green) and across-track (black) tidal velocities derived through harmonic analysis.

Significant spatial and temporal variability is observed in the hydrographic properties along ALR's track. This variability is strongly related to the observed horizontal tidal advection (Figure 3). For the first 5 hours of ALR's mission, along-track tidal advection is directed into the cavity and the water column along the AUV track is dominated by a combination of fresh surface waters and MWDW (Figures 6d and 7b). No signature of the densest HSSW is observed until ALR reaches 15 km from the ice front (Figures 6a and 6b), as this water mass has been advected further into the ice shelf cavity by the horizontal tidal flow and replaced by lighter water masses behind. By the time ALR reaches its turning point, however, the along-track tidal flow has reversed and is running at maximum velocity toward the ice front (Figure 6d). HSSW from deeper within the ice shelf cavity has increasingly been advected toward the ice front, displacing the lighter water masses observed by ALR at the beginning of its mission (Figure 7c, Figures 6a and 6b). Despite following the same geographical path as the outbound leg, the water column during the return portion of ALR's mission is entirely dominated by mixtures of dense HSSW and MWDW to within 5 km of the ice front, with a complete absence of the lightest surface waters previously observed. The patch of warmest MWDW that is observed ~11 km from the ice front on ALR's outbound leg has been displaced ~5–6 km toward the ice front (Figure 6a), consistent with the tidal advection distance calculated for the portion of ALR's mission that the along-track tidal current was directed out of the ice shelf cavity. It is possible that some of the variability observed in the hydrographic properties along ALR's track is due to vertical heave, as eastwards across-track tidal current flows up the eastern flank of the Central Trough and raises the height of the densest HSSW above the seabed. However, for the period of time that the along-track tidal current is flowing out of the ice shelf cavity and the water column is becoming denser, the across-track current is directed toward the west (Figures 4a and 6d) in the down-slope direction (Figures 1a and 2), which would tend to depress

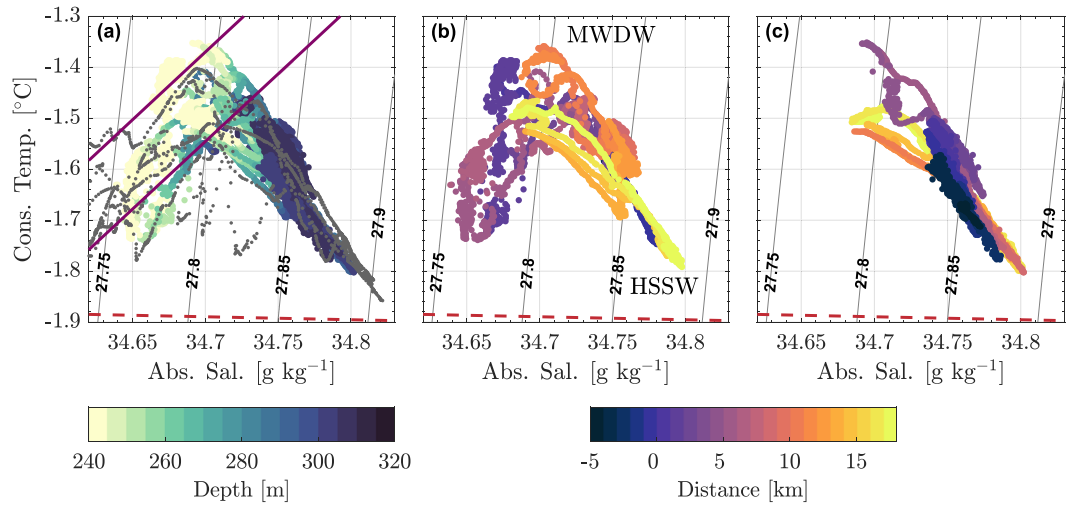


**Figure 7.** Conservative Temperature-Absolute Salinity diagrams for (a) the entire ALR mission, (b) the outbound leg of ALR's mission, and (c) the return leg of ALR's mission colored as a function of depth in (a) and distance from the ice front (positive into the cavity) in (b) and (c). The red dashed line in each panel shows the surface freezing point as a function of salinity. In (a) the small gray dots show data from ship-based CTD casts at the ice front, while the purple lines show meltwater mixing lines along which a MWDW water mass would evolve as it interacts with the ice base and drives basal melting. The background contours in each panel show sigma-t referenced to the sea surface. MWDW refers to Modified Warm Deep Water and HSSW refers to High Salinity Shelf Water.

rather than raise the height of HSSW. Furthermore, with a slope angle of only 0.18° and a total across-track tidal advection of 3.7 km, the effect of the tides interacting with the eastern flank would be limited to a vertical displacement of <12 m. Vertically integrating the thermal wind balance indicates that the horizontal density gradient ($3.3 \pm 0.7 \times 10^{-3}$ kg m$^{-3}$ km$^{-1}$) between the lighter waters observed close to the ice front and the denser HSSW observed at ALR's turnaround point (Figure 6) can drive south-eastwards across-track geostrophic shear of up to 1 cm s$^{-1}$ over the depth range covered by ALR, however this increases to 5 cm s$^{-1}$ if the horizontal density gradient is integrated over the mean water column thickness (241 m).

### 3.3. Microstructure

Background mixing rates ($\varepsilon$ and $\chi$) along ALR's track are weak. $\varepsilon$ and $\chi$ average $1.7 \times 10^{-10}$ W kg$^{-1}$ and $1.2 \times 10^{-10}$ °C$^2$ s$^{-1}$, respectively, with 81% and 77% of observed values less than $10^{-9}$ W kg$^{-1}$ and $10^{-9}$ °C$^2$ s$^{-1}$ (Figures 8a and 8b). Where vertical profiles are available, $\varepsilon$ and $\chi$ tend to decrease with depth, reaching a minimum of $10^{-11}$ W kg$^{-1}$ or °C$^2$ s$^{-1}$ below 300 m (Figure 10a). Background mixing rates are similar to those observed away from the boundaries beneath Pine Island Ice Shelf (Kimura et al., 2016) and are equivalent to open-ocean background levels. They are consistently lower than those observed in shear-driven ice shelf-ocean boundary layers (Davis & Nicholls, 2019) or beneath fast ice (Inall et al., 2022), and tend to indicate that despite the tidal forcing, the region of the cavity sampled by ALR is relatively quiescent (at least during neap tides). Over the depth range covered by the vehicle, there is no evidence of $\varepsilon$ and $\chi$ scaling with the mean flow speed, or of an increase in mixing at the ice front where the flow is required to navigate the topographic step imposed by the ice shelf. Instead, the highest rates of $\varepsilon$ and $\chi$ are observed within the warm pulse of MWDW that is seen ~11 and ~5 km from the ice front on the outbound and return legs, respectively. Here, stronger horizontal temperature gradients and elevated shear motion drive observed rates of mixing that are two orders of magnitude higher than the average background value ($\varepsilon \sim 10^{-8}$ W kg$^{-1}$ and $\chi \sim 10^{-8}$ °C$^2$ s$^{-1}$), which will actively contribute to diffusing and eroding the warm MWDW signature. $\varepsilon$ and $\chi$ are linearly correlated in log-log space (Figures 9a and 10a), indicating that regions of high shear correspond to regions of high temperature gradient microstructure and mixing is likely driven by shear-generated turbulence (Inoue et al., 2007). In contrast, if double diffusive effects were dominant, we would expect to observe high temperature gradients at temperature steps, with negligible shear microstructure. The buoyancy Reynolds number

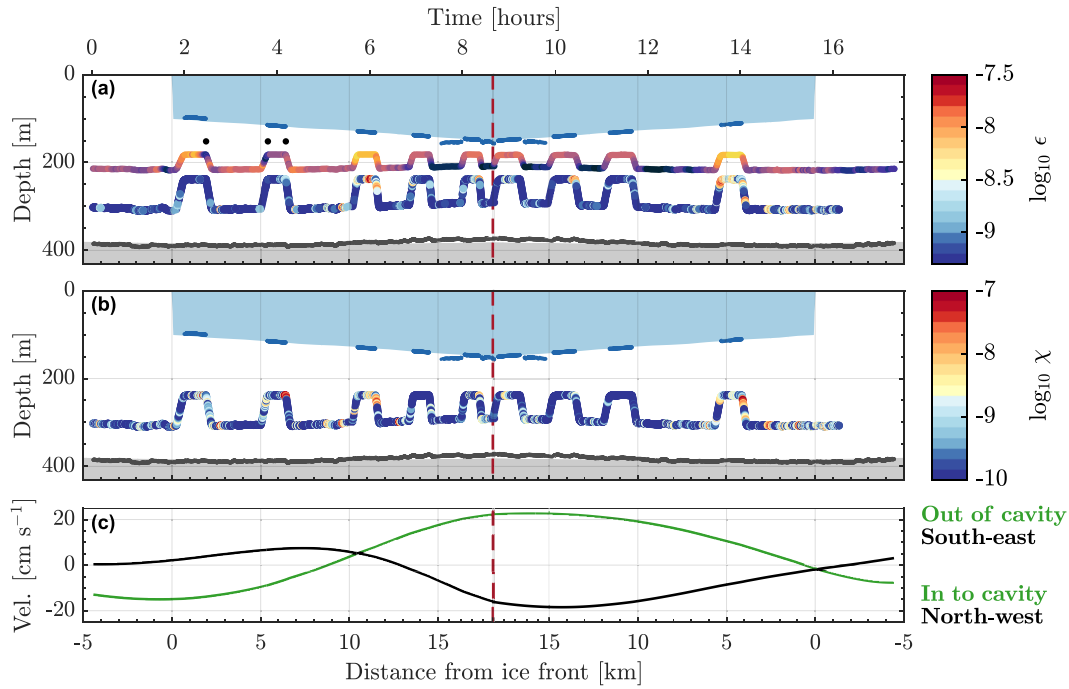


**Figure 8.** The rate of (a) turbulent kinetic energy dissipation ε and (b) thermal variance dissipation χ along ALR's track plotted in the same format as Figure 3. (c) along-track (green) and across-track (black) tidal velocities derived through harmonic analysis. Conservative temperature along ALR's track is plotted in (a) for comparison with ε and χ. For display purposes, the vehicle track for conservative temperature has been shifted 80 m in the vertical and the depth range has been scaled by a factor of 0.5. The color scale matches that in Figure 6a. The black dots mark the water column profiles where Θ increases with depth and therefore the water column is susceptible to diffusive convection.

$$R_\varepsilon = \frac{\varepsilon}{\upsilon \overline{N}^2}, \tag{10}$$

relates the strength of the turbulence characterized by the TKE dissipation, to the strength of the stratification characterized by the background buoyancy frequency (Gargett, 1988). When $R_\varepsilon > 20$ the water column is assumed to be fully turbulent, whereas when $R_\varepsilon < 20$ turbulence is suppressed by stratification. Observed values of $R_\varepsilon$ are greater than 20 for only a relatively small proportion of the water column covered by ALR (i.e., shallower than 255–260 m; Figure 10b), whereas deeper than this $R_\varepsilon$ is less than 20 everywhere indicating that turbulence is not fully developed. Even if the four water column profiles which sample the MWDW pulse and exhibit the highest values of ε are excluded, the average value of $R_\varepsilon$ remains >20 for depths shallower than 255–260 m. Thus, enhanced turbulence along the upper portion of ALR's track is a consistent feature throughout the mission. In contrast, turbulence suppression deeper than 255–260 m (Figure 8a) indicates that the HSSW layer is characterized by both weak shear motion and weak horizontal temperature gradients, consistent with the very low levels of TKE and thermal variance dissipation observed here.

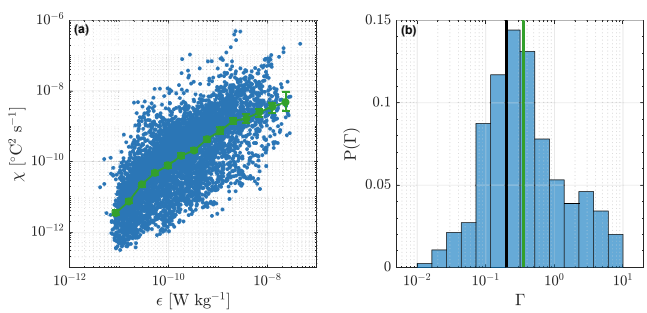


**Figure 9.** (a) The rate of turbulent kinetic energy dissipation plotted against the rate of thermal variance dissipation. The green dotted line shows mean values of χ with 95% confidence intervals in equally log-spaced ε bins. (b) Probability histogram for the mixing efficiency along ALR's track. The vertical black line marks the canonical value Γ = 0.2, while the vertical green line marks the median value Γ = 0.35 observed by ALR.

Calculated values of Γ beneath Ronne Ice Shelf vary by up to three orders of magnitude from $10^{-2}$ to $10^{1}$ ($Ri_f \approx 10^{-2}$ to 0.9; Figure 9b). The median value of Γ, however, does not differ significantly from the canonical value of 0.2. The average eddy diffusivity $K_\rho$ reaches ~$10^{-4}$ m$^2$ s$^{-1}$ for the upper levels of ALR's track where the water column is fully turbulent (Figure 10c), while deeper than 260 m, $K_\rho$ decreases by up to two orders of magnitude reaching a minimum value of $10^{-5}$ to $10^{-6}$ m$^2$ s$^{-1}$. Over the depth range covered by ALR's mission track, turbulent mixing drives a downward (negative) vertical heat flux from the MWDW layer that averages 0.2 W m$^{-2}$ (Figure 10d).

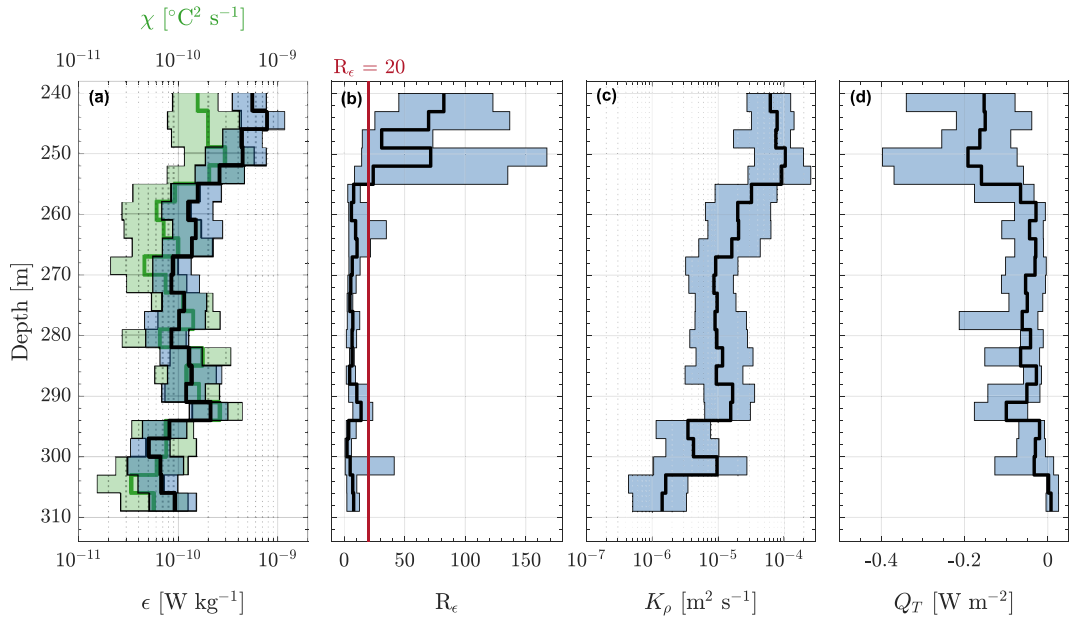


**Figure 10.** Average vertical profiles of (a) the rate of turbulent kinetic energy dissipation ε (black) and the rate of thermal variance dissipation χ (green), (b) the buoyancy Reynolds number, (c) the vertical eddy diffusivity, and (d) the vertical heat flux where a negative flux is directed downwards. The red line in (b) marks $R_\epsilon = 20$, below which shear driven turbulence is suppressed by stratification. The error bars in (a) – (d) were estimated using a bootstrapping procedure (Rippeth & Inall, 2002).

Upward (positive) vertical heat fluxes from the MWDW layer are also likely to be significant, however, their magnitude cannot be determined directly due to the lack of coverage by ALR (see Section 4). For the region of the water column where turbulence is suppressed by stratification, the vertical heat flux tends toward a magnitude of $<-0.1$ W m$^{-2}$. In contrast to $K_\rho$, the vertical temperature gradient (not shown) increases with depth and is an order of magnitude steeper in the HSSW layer than in the lighter surface layers. A steeper temperature gradient should strengthen the vertical heat flux with depth, in contrast to what is observed (Figure 10d). Thus, variability in the vertical heat flux appears to be controlled primarily by variation in $K_\rho$, which decreases by 2 orders of magnitude with depth (Figure 10b).

## 4. Discussion and Conclusions

Using the Autosub Long Range (ALR) autonomous underwater vehicle, we have described the first hydrographic, velocity and microstructure observations along the MWDW inflow beneath Ronne Ice Shelf (Figures 1 and 2). ALR spent 13.9 hours beneath the ice, reaching a maximum distance of 18.2 km from the ice front. Along ALR's track, the ice shelf cavity was dominated by the presence of light and fresh surface waters, Modified Warm Deep Water (MWDW) and dense and cold High Salinity Shelf Water (Figure 6). A particularly warm, isolated pulse of MWDW that was warmer than any MWDW observed outside of the ice shelf cavity from concurrent ship-based data (Figure 7), was observed on the outbound and return leg. Our observations suggest that the inflow of the warmest MWDW is sporadic, which is consistent with long-term data from ocean moorings deployed just outside of the Ronne cavity (Foldvik et al., 2001). The patchiness could be related to either the varying levels of heat loss experienced by parcels of MWDW as they transit across the Weddell Sea continental shelf or is a signature of eddy-related activity driving cross-ice shelf front exchange (Årthun et al., 2013). While no clear cyclonic or anti-cyclonic rotating vortex-like structures that would indicate eddy activity were seen in the ADCP velocity data, the snapshot nature of ALR's observations make them particularly difficult to detect unless the mission track bisected the eddy feature directly through its center (Figure 5). In addition, as the MWDW signature at the ice front is at least 150 km wide (Figure 2a), the position of the warmest inflow along the Ronne Ice Front may evolve in time, generating the observed patchiness seen in both the ALR data and the fixed moorings used in Foldvik et al. (2001). Determining the ultimate source of this patchiness requires further field observations.

Current velocities along the MWDW inflow are dominated by the tides, with the maximum tidal speed (during neap tides) reaching 29 cm $s^{-1}$ (Figure 3). Along-track tidal advection plays a critical role in setting the temporal/spatial variability in the hydrographic properties observed by ALR. During the outbound leg, tidal advection is directed into the cavity and the water column is dominated by light surface water and MWDW. In contrast, when the along-track tidal current switches direction, dense HSSW from deeper in the cavity is advected toward the ice front and displaces the lighter waters seen previously. Despite the large tidal excursion (5.6 km), a persistent south-westward detided flow of MWDW is observed with a core current speed of 4.0 cm $s^{-1}$ (Figure 5). The inflow of warm MWDW provides a substantial source of heat for basal melting, which can be readily seen in satellite derived products (Figure 1a), and the maximum thermal driving along the vehicle track (~0.6°C). While upward vertical heat fluxes toward the ice base are likely to be significant, their magnitude cannot be determined directly as ALR did not sample the upper part of the MWDW inflow closest to the ice base. An indirect estimate of the basal melt rate can be derived by considering the difference between the ice thickness derived from the ALR ice draft observations (assuming a water-ice density ratio of 1.12) and ice thickness from Bedmap2. After horizontally displacing the Bedmap2 data in the along-track direction by 20 km, such that it aligns with the 2018 ice front position, a uniform thinning of ~74 m was applied to match the ALR-derived ice thickness. As ice thickness in Bedmap2 was determined from satellite-based observations between 1994 and 1995 (Griggs & Bamber, 2011), this implies a mean thinning rate along ALR's track of ~3 m $yr^{-1}$. The combined effect of surface accumulation (200–250 kg $m^{-2}$ $yr^{-1}$ or ~0.27 m $yr^{-1}$ ice equivalent thickening) and the vertical strain rate ($2 \times 10^{-3}$ $yr^{-1}$ or ~0.30 m $yr^{-1}$ of thinning; Jenkins & Doake, 1991) effectively provides no net contribution, and therefore the 3 m $yr^{-1}$ thinning rate along ALR's track can be interpreted entirely as a basal melt rate, which is consistent with contemporary satellite-derived estimates (Figure 1a; Adusumilli et al., 2020). Basal melting is driven by the divergence of the sensible heat flux at the ice-ocean interface (Davis & Nicholls, 2019; Jenkins et al., 2010) and thus the vertical heat flux, $Q_T$, from the MWDW layer required to maintain the basal melt rate is given by

$$Q_T = \rho_i L_i \dot{m} - K_i \frac{\partial T_i}{\partial z}, \tag{11}$$

where $\rho_i$ is ice density, $L_i$ is the latent heat of fusion of ice, $\dot{m}$ is the basal melt rate, $K_i$ is the thermal conductivity of ice ($K_i = \rho_i c_i \kappa_i^T$, where $c_i$ is the specific heat capacity of ice and $\kappa_i^T$ is the thermal diffusivity of ice), and $\partial T_i / \partial z$ is the ice base temperature gradient. Using canonical parameters from Jenkins et al. (2010), the vertical heat flux is ~28 W $m^{-2}$.

The inflow of warm MWDW observed here is likely to be seasonal. In winter brine rejection from sea ice formation drives convection that cools the water column to the surface freezing point and entirely erodes the MWDW layer by austral spring (Foldvik et al., 2001). For this predominantly barotropic water column, the step in water column thickness at the ice front further becomes a potential vorticity barrier that prevents an inflow into the ice shelf cavity (Årthun et al., 2013; Grosfeld et al., 1997; Wåhlin et al., 2020). In contrast, summer stratification helps isolate the lower water column from this dynamic barrier, facilitating baroclinic flow across the ice front. Even in the presence of this stratification, however, Darelius et al. (2014) and Wåhlin et al. (2020) show that the ice front step in water column thickness continues to restrict barotropic cross-ice front flow. Darelius et al. (2014) observed that the gradient in potential vorticity (i.e., water column thickness) across the Filchner Ice Front caused southward barotropic flow toward the ice shelf to turn toward the west and flow parallel to the ice front, while northward flow out of the Filchner cavity was turned partially toward the east. A south-eastward across-track flow parallel to the Ronne ice front was observed by ALR with a mean current velocity of 4.8 cm $s^{-1}$ (Figure 5). While the magnitude of this flow is consistent with the strength of the along-track horizontal density gradient, its position ~5 km inward of the ice front is noticeably unaffected by horizontal tidal advection and the loss of light surface waters from the cavity during ALR's outbound leg. This observation leads us to speculate that part of this flow may be dynamically linked to the fixed presence of the ice front and steering of barotropic currents. If the south-westward flow of MWDW across the Weddell Sea continental shelf has a significant barotropic component (like many flows toward ice shelf cavities, e.g., Assmann et al., 2019; Kalén et al., 2016), the barotropic part of the inflow will be turned toward the north-west as it interacts with the Ronne ice front. The 5 cm $s^{-1}$ south-eastward baroclinic geostrophic velocity shear will be superimposed upon this barotropic current, driving a net flow to the south-east as observed by ALR. Conversely, ship-based CTD sections in front of Ronne Ice Shelf show that Ice Shelf Water flows out of the cavity to the north-west of ALR's track along the eastern flank of the

Ronne Depression (Janout et al., 2021). As this flow navigates the ice front topographic step, a proportion may be turned to the south-east which then crosses ALR's track in the vicinity of the ice front. While the drivers of the across-track circulation observed by ALR remain uncertain from the data available, it has significant implications for ocean heat fluxes and basal melting and is therefore worthy of further investigation. Combining traditional fixed moorings with further AUV missions and data gathered from autonomous floats and gliders that repeatedly cross the topographic step would be a useful approach to understand these ice front processes and their evolution year-round.

The rates of turbulent mixing along ALR's track are relatively weak, with average values of $\varepsilon$ and $\chi$ no higher than background open-ocean rates ($1.7 \times 10^{-10}$ W kg$^{-1}$ and $1.2 \times 10^{-10}$ °C$^2$ s$^{-1}$, respectively; Figure 8). Low levels of mixing are consistent with the relatively large distance between ALR's track and the ice base/seabed and the absence of the strongest shear-driven turbulence that originates from the boundaries. The turbulence observations suggest that despite the proximity of ALR's track to the critical latitude for the semi-diurnal tides, vertical tidal current shear away from the boundaries is relatively weak, which is consistent with the ADCP data that show predominantly barotropic tidal currents and no evidence of thick tidal boundary layers (Figure 3; Makinson, 2002; Makinson et al., 2006). Deeper than 255 m the buoyancy Reynolds number is less than 20, indicating that turbulence is readily suppressed by stratification (Figure 10). The highest rates of mixing are associated with the warmest pulse of MWDW, with $\varepsilon$ and $\chi$ reaching $\sim 10^{-8}$ W kg$^{-1}$ and °C$^2$ s$^{-1}$, respectively (Figure 8). While it remains unclear from ALR's single mission whether the inflow of MWDW beneath Ronne Ice Shelf is persistently characterized by high rates of dissipation, such behavior would contribute to rapid diffusion of the MWDW signature beneath the ice shelf and may play a role in limiting its geographic extent. Consistent with previous studies (e.g., Bluteau et al., 2017), the observed mixing efficiency spans three orders of magnitude but has a median value close to the canonical value used in geophysical studies of 0.2 (Figure 9b). Where the water column is fully turbulent, the vertical eddy diffusivity reaches $10^{-4}$ m$^2$ s$^{-1}$ (Figure 10). Observed diffusivity is up to two orders of magnitude higher than the standard values used in numerical models of ice shelf cavities (e.g., Hausmann et al., 2020; Jourdain et al., 2017), and these observations will provide a unique benchmark against which different numerical models can be compared and tuned. Over the depth range covered by ALR, the eddy diffusivity drives a downward vertical heat flux that reaches an average of 0.2 W m$^{-2}$, contributing to warming the dense and cold Berkner-derived HSSW found at depth in the Central Trough (Figure 10). This downward vertical heat flux is significantly smaller than the estimated upward vertical heat flux required to drive the estimated basal melt rate, indicating that the diffusivity either increases close to the ice base, and/or the temperature gradient in the upper MWDW layer is sharper.

ALR's mission beneath Ronne Ice Shelf provides a unique snapshot of the hydrographic, velocity, and microstructure properties along the MWDW inflow. Many open questions remain, however, that cannot be answered with the data available here. For example, the eventual fate of the MWDW inflow beneath Ronne Ice Shelf remains unclear, and we don't understand fully the impact of the MWDW inflow on basal melting and ice shelf mass loss. There is no evidence of MWDW deeper in the cavity (Nicholls et al., 2001, 2004), and the patch of elevated basal melting remains geographically restricted to the ice front. Some models indicate that the MWDW inflow may recirculate close to the ice front in a gyre-type circulation (Hausmann et al., 2020; Makinson & Nicholls, 1999), although observations remain sparse. Furthermore, the different mechanisms by which the MWDW inflow navigates the ice front step in water column thickness throughout the year and different stratification environments requires further investigation. While Ronne-Filchner Ice Shelf currently remains isolated from large-scale warm water inflow, MWDW may come to dominate the cavity under future climate change scenarios (Hellmer et al., 2012; Naughten et al., 2021). Thus, there is strong motivation to use further high spatial and temporal resolution autonomous vehicle surveys in conjunction with the longer-term temporal information that can only be provided traditional sub-ice-shelf mooring arrays (e.g., Hattermann et al., 2021) to investigate these outstanding questions, and ultimately build a complete understanding of the dynamics that govern the inflow, circulation and fate of MWDW beneath Ronne Ice Shelf.

## Data Availability Statement

Hydrographic, velocity and turbulence data from Autosub Long Range are available from the UK Polar Data Centre (doi: 10.5285/eb2f66fa-1c64-49af-b9e8-ce3124ce3c03). CTD data from the PS111 cruise are available from PANGAEA (doi: 10.1594/PANGAEA.897280).

**Acknowledgments**
Autosub Long Range beneath Filchner-Ronne Ice Shelf was funded by the UK Natural Environment Research Council Large Grant "Ice shelves in a warming world: Filchner Ice Shelf system, Antarctica" (Grant Number NE/L013770/1). This study uses data provided by the Alfred Wegener Institute Helmholtz-Centre for Polar- and Marine Research in Bremerhaven (Grant Number AWI-PS111_01). The authors thank Captain Schwarze and the crew of RV *Polarstern* for the support during PS111.

## References

Adusumilli, S., Fricker, H. A., Medley, B., Padman, L., & Siegfried, M. R. (2020). Interannual variations in meltwater input to the Southern Ocean from Antarctic ice shelves. *Nature Geoscience*, *13*(9), 616–620. https://doi.org/10.1038/s41561-020-0616-z

Akhoudas, C., Sallée, J., Reverdin, G., Aloisi, G., Benetti, M., Vignes, L., & Gelado, M. (2020). Ice Shelf Basal Melt and Influence on Dense Water Outflow in the Southern Weddell Sea. *Journal of Geophysical Research: Oceans*, *125*(2). https://doi.org/10.1029/2019JC015710

Allen, J. T. (1995). Subtidal and Tidal Currents in the Vicinity of the Iceland-Færœs Front. *Journal of Atmospheric and Oceanic Technology*, *12*(3), 567–588. https://doi.org/10.1175/1520-0426(1995)012<0567:satcit>2.0.co;2

Arndt, J. E., Schenke, H. W., Jakobsson, M., Nitsche, F. O., Buys, G., Goleby, B., et al. (2013). The International Bathymetric Chart of the Southern Ocean (IBCSO) Version 1.0-A new bathymetric compilation covering circum-Antarctic waters. *Geophysical Research Letters*, *40*, 3111–3117. https://doi.org/10.1002/grl.50413

Årthun, M., Holland, P. R., Nicholls, K. W., & Feltham, D. L. (2013). Eddy-Driven Exchange between the Open Ocean and a Sub–Ice Shelf Cavity. *Journal of Physical Oceanography*, *43*(11), 2372–2387. https://doi.org/10.1175/JPO-D-13-0137.1

Årthun, M., Nicholls, K. W., Makinson, K., Fedak, M. A., & Boehme, L. (2012). Seasonal inflow of warm water onto the southern Weddell Sea continental shelf, Antarctica. *Geophysical Research Letters*, *39*(17), L17601. https://doi.org/10.1029/2012GL052856

Assmann, K. M., Darelius, E., Wåhlin, A. K., Kim, T. W., & Lee, S. H. (2019). Warm Circumpolar Deep Water at the Western Getz Ice Shelf Front, Antarctica. *Geophysical Research Letters*. https://doi.org/10.1029/2018GL081354

AWI. (2017). Polar Research and Supply Vessel POLARSTERN operated by the Alfred-Wegener-Institute. *Journal of Large-Scale Research Facilities JLSRF*, *3*, A119. https://doi.org/10.17815/jlsrf-3-163

Bluteau, C. E., Jones, N. L., & Ivey, G. N. (2013). Turbulent mixing efficiency at an energetic ocean site. *Journal of Geophysical Research: Oceans*, *118*(9), 4662–4672. https://doi.org/10.1002/jgrc.20292

Bluteau, C. E., Jones, N. L., & Ivey, G. N. (2016). Estimating Turbulent Dissipation from Microstructure Shear Measurements Using Maximum Likelihood Spectral Fitting over the Inertial and Viscous Subranges. *Journal of Atmospheric and Oceanic Technology*, *33*, 713–722. https://doi.org/10.1175/JTECH-D-15-0218.1

Bluteau, C. E., Lueck, R. G., Ivey, G. N., Jones, N. L., Book, J. W., & Rice, A. E. (2017). Determining Mixing Rates from Concurrent Temperature and Velocity Measurements. *Journal of Atmospheric and Oceanic Technology*, *34*(10), 2283–2293. https://doi.org/10.1175/JTECH-D-16-0250.1

Carmack, E. C. (1974). A quantitative characterization of water masses in the Weddell Sea during summer. *Deep Sea Research and Oceanographic Abstracts*, *21*(6), 431–443. https://doi.org/10.1016/0011-7471(74)90092-8

Daae, K., Hattermann, T., Darelius, E., Mueller, R. D., Naughten, K. A., Timmermann, R., & Hellmer, H. H. (2020). Necessary Conditions for Warm Inflow Toward the Filchner Ice Shelf, Weddell Sea. *Geophysical Research Letters*, *47*(22). https://doi.org/10.1029/2020GL089237

Darelius, E., Fer, I., & Nicholls, K. W. (2016). Observed vulnerability of Filchner-Ronne Ice Shelf to wind-driven inflow of warm deep water. *Nature Communications*, *7*, 12300. https://doi.org/10.1038/ncomms12300

Darelius, E., Makinson, K., Daae, K., Fer, I., Holland, P. R., & Nicholls, K. W. (2014). Hydrography and circulation in the Filchner Depression, Weddell Sea, Antarctica. *Journal of Geophysical Research: Oceans*, *119*(9), 5797–5814. https://doi.org/10.1002/2014JC010225

Darelius, E., & Sallée, J. B. (2018). Seasonal Outflow of Ice Shelf Water Across the Front of the Filchner Ice Shelf, Weddell Sea, Antarctica. *Geophysical Research Letters*, *45*(8), 3577–3585. https://doi.org/10.1002/2017GL076320

Davis, P. E. D., & Nicholls, K. W. (2019). Turbulence Observations Beneath Larsen C Ice Shelf, Antarctica. *Journal of Geophysical Research*, *124*(8), 5529–5550. https://doi.org/10.1029/2019JC015164

Foldvik, A., Gammelsrød, T., Nygaard, E., & Østerhus, S. (2001). Current measurements near Ronne Ice Shelf: Implications for circulation and melting. *Journal of Geophysical Research*, *106*, 4463–4477. https://doi.org/10.1029/2000JC000217

Foldvik, A., Gammelsrød, T., & Tørresen, T. (1985). Circulation and water masses on the southern Weddell Sea shelf. In S. S. Jacobs (Ed.), *Oceanology of the Antarctic Continental Shelf, Antarctic Research Series 43* (pp. 5–20). American Geophysical Union. https://doi.org/10.1029/AR043p0005

Fretwell, P., Pritchard, H. D., Vaughan, D. G., Bamber, J. L., Barrand, N. E., Bell, R., et al. (2013). Bedmap2: Improved ice bed, surface and thickness datasets for Antarctica. *The Cryosphere*, *7*, 375–393. https://doi.org/10.5194/tc-7-375-2013

Fürst, J. J., Durand, G., Gillet-Chaulet, F., Tavard, L., Rankl, M., Braun, M., & Gagliardini, O. (2016). The safety band of Antarctic ice shelves. *Nature Climate Change*, *6*, 479–482. https://doi.org/10.1038/nclimate2912

Gade, H. H. (1979). Melting of Ice in Sea Water: A Primitive Model with Application to the Antarctic Ice Shelf and Icebergs. *Journal of Physical Oceanography*, *9*(1), 189–198. https://doi.org/10.1175/1520-0485(1979)009<0189:moiisw>2.0.co;2

Gammelsrød, T., & Slotsvik, N. (1981). Hydrographie and Current Measurements in the Southern Weddell Sea 1979/80. *Polarforschung*, *51*(1), 101–111.

Gardner, A. S., Moholdt, G., Scambos, T., Fahnstock, M., Ligtenberg, S., van den Broeke, M., & Nilsson, J. (2018). Increased West Antarctic and unchanged East Antarctic ice discharge over the last 7 years. *The Cryosphere*, *12*(2), 521–547. https://doi.org/10.5194/tc-12-521-2018

Gargett, A. E. (1988). The scaling of turbulence in the presence of stable stratification. *Journal of Geophysical Research*, *93*(C5), 5021. https://doi.org/10.1029/JC093iC05p05021

Griggs, J. A., & Bamber, J. L. (2011). Antarctic ice-shelf thickness from satellite radar altimetry. *Journal of Glaciology*, *57*(203), 485–498. https://doi.org/10.3189/002214311796905659

Grosfeld, K., Gerdes, R., & Determann, J. (1997). Thermohaline circulation and interaction between ice shelf cavities and the adjacent open ocean. *Journal of Geophysical Research*, *102*(C7), 15595–15610. https://doi.org/10.1029/97JC00891

Haid, V., & Timmermann, R. (2013). Simulated heat flux and sea ice production at coastal polynyas in the southwestern Weddell Sea. *Journal of Geophysical Research: Oceans*, *118*(5), 2640–2652. https://doi.org/10.1002/jgrc.20133

Hattermann, T. (2018). Antarctic Thermocline Dynamics along a Narrow Shelf with Easterly Winds. *Journal of Physical Oceanography*, *48*(10), 2419–2443. https://doi.org/10.1175/JPO-D-18-0064.1

Hattermann, T., Nicholls, K. W., Hellmer, H. H., Davis, P. E. D., Janout, M. A., Østerhus, S., et al. (2021). Observed interannual changes beneath Filchner-Ronne Ice Shelf linked to large-scale atmospheric circulation. *Nature Communications*, *12*(1), 2961. https://doi.org/10.1038/s41467-021-23131-x

Hausmann, U., Sallée, J., Jourdain, N. C., Mathiot, P., Rousset, C., Madec, G., et al. (2020). The Role of Tides in Ocean-Ice Shelf Interactions in the Southwestern Weddell Sea. *Journal of Geophysical Research: Oceans*, *125*(6). https://doi.org/10.1029/2019JC015847

Hellmer, H. H., Jacobs, S. S., & Jenkins, A. (1998). Oceanic Erosion of a Floating Antarctic Glacier in the Amundsen Sea. In S. S. Jacobs & R. F. Weiss (Eds.), *Antarctic Research Series* (pp. 83–99). American Geophysical Union. https://doi.org/10.1029/AR075p0083

Hellmer, H. H., Kauker, F., Timmermann, R., Determann, J., & Rae, J. (2012). Twenty-first-century warming of a large Antarctic ice-shelf cavity by a redirected coastal current. *Nature*, *485*, 225–228. https://doi.org/10.1038/nature11064

Hellmer, H. H., Kauker, F., Timmermann, R., & Hattermann, T. (2017). The Fate of the Southern Weddell Sea Continental Shelf in a Warming Climate. *Journal of Climate*, *30*, 4337–4350. https://doi.org/10.1175/JCLI-D-16-0420.1

IMBIE. (2018). Mass balance of the Antarctic Ice Sheet from 1992 to 2017. *Nature*, *558*(7709), 219–222. https://doi.org/10.1038/s41586-018-0179-y

Inall, M. E., Brearley, J. A., Henley, S. F., Fraser, A. D., & Reed, S. (2022). Landfast Ice Controls on Turbulence in Antarctic Coastal Seas. *Journal of Geophysical Research: Oceans*, *127*(1). https://doi.org/10.1029/2021JC017963

Inoue, R., Yamazaki, H., Wolk, F., Kono, T., & Yoshida, J. (2007). An Estimation of Buoyancy Flux for a Mixture of Turbulence and Double Diffusion. *Journal of Physical Oceanography*, *37*, 611–624. https://doi.org/10.1175/JPO2996.1

Jacobs, S. S., Hellmer, H. H., & Jenkins, A. (1996). Antarctic Ice Sheet melting in the southeast Pacific. *Geophysical Research Letters*, *23*, 957–960. https://doi.org/10.1029/96GL00723

Janout, M. A., Hellmer, H. H., Hattermann, T., Huhn, O., Sültenfuss, J., Østerhus, S., et al. (2021). FRIS Revisited in 2018: On the Circulation and Water Masses at the Filchner and Ronne Ice Shelves in the Southern Weddell Sea. *Journal of Geophysical Research: Oceans*, *126*(6). https://doi.org/10.1029/2021JC017269

Janout, M. A., Hellmer, H. H., Schröder, M., & Wisotzki, A. (2019). Physical oceanography during POLARSTERN cruise PS111 (ANT-XXXIII/2). *Alfred Wegener Institute, Helmholtz Centre for Polar and Marine Research, Bremerhaven, PANGAEA*.

Jenkins, A., & Doake, C. S. M. (1991). Ice-ocean interaction on Ronne Ice Shelf, Antarctica. *Journal of Geophysical Research*, *96*(C1), 791–813. https://doi.org/10.1029/90jc01952

Jenkins, A., Dutrieux, P., Jacobs, S., Steig, E., Gudmundsson, H., Smith, J., & Heywood, K. (2016). Decadal Ocean Forcing and Antarctic Ice Sheet Response: Lessons from the Amundsen Sea. *Oceanography*, *29*, 106–117. https://doi.org/10.5670/oceanog.2016.103

Jenkins, A., Nicholls, K. W., & Corr, H. F. J. (2010). Observation and Parameterization of Ablation at the Base of Ronne Ice Shelf, Antarctica. *Journal of Physical Oceanography*, *40*, 2298–2312. https://doi.org/10.1175/2010JPO4317.1

Jourdain, N. C., Mathiot, P., Merino, N., Durand, G., Le Sommer, J., Spence, P., et al. (2017). Ocean circulation and sea-ice thinning induced by melting ice shelves in the Amundsen Sea. *Journal of Geophysical Research*, *122*, 2550–2573. https://doi.org/10.1002/2016JC012509

Kalén, O., Assmann, K. M., Wahlin, A. K., Ha, H. K., Kim, T. W., & Lee, S. H. (2016). Is the oceanic heat flux on the central Amundsen sea shelf caused by barotropic or baroclinic currents? *Deep Sea Research Part II: Topical Studies in Oceanography*, *123*, 7–15. https://doi.org/10.1016/j.dsr2.2015.07.014

Kimura, S., Jenkins, A., Dutrieux, P., Forryan, A., Naveira Garabato, A. C., & Firing, Y. (2016). Ocean mixing beneath Pine Island Glacier ice shelf, West Antarctica. *Journal of Geophysical Research*, *121*, 8496–8510. https://doi.org/10.1002/2016JC012149

Levine, E. R., & Lueck, R. G. (1999). Turbulence Measurement from an Autonomous Underwater Vehicle. *Journal of Atmospheric and Oceanic Technology*, *16*(11), 1533–1544. https://doi.org/10.1175/1520-0426(1999)016<1533:tmfaau>2.0.co;2

Lewis, E. L., & Perkin, R. G. (1986). Ice pumps and their rates. *Journal of Geophysical Research*, *91*(C10), 11756. https://doi.org/10.1029/JC091iC10p11756

Lueck, R. (2016). *Calculating the Rate of Dissipation of Turbulent Kinetic Energy* (p. 19). RSI Technical Note No. 028.

Macoun, P., & Lueck, R. (2004). Modeling the Spatial Response of the Airfoil Shear Probe Using Different Sized Probes. *Journal of Atmospheric and Oceanic Technology*, *21*(2), 284–297. https://doi.org/10.1175/1520-0426(2004)021<0284:mtsrot>2.0.co;2

Makinson, K. (2002). Modeling tidal current propdfs and vertical mixing beneath Filchner–Ronne Ice Shelf, Antarctica. *Journal of Physical Oceanography*, *32*, 202–215. https://doi.org/10.1175/1520-0485(2002)032<0202:mtcpav>2.0.co;2

Makinson, K., & Nicholls, K. W. (1999). Modeling tidal currents beneath Filchner-Ronne Ice Shelf and on the adjacent continental shelf: Their effect on mixing and transport. *Journal of Geophysical Research*, *104*(C6), 13449–13465. https://doi.org/10.1029/1999JC900008

Makinson, K., Schroder, M., & Osterhus, S. (2006). Effect of critical latitude and seasonal stratification on tidal current profiles along Ronne Ice Front, Antarctica. *Journal of Geophysical Research*, *111*(C03022), 1–15. https://doi.org/10.1029/2005JC003062

McDougall, T. J., & Barker, P. M. (2011). Getting started with TEOS-10 and the Gibbs Seawater (GSW) Oceanographic Toolbox. SCOR/IAPSO WG127Retrieved from https://teos-10.org/pubs/Getting_Started.pdf

McDougall, T. J., Barker, P. M., Feistel, R., & Galton-Fenzi, B. K. (2014). Melting of Ice and Sea Ice into Seawater and Frazil Ice Formation. *Journal of Physical Oceanography*, *44*(7), 1751–1775. https://doi.org/10.1175/JPO-D-13-0253.1

Naughten, K. A., De Rydt, J., Rosier, S. H. R., Jenkins, A., Holland, P. R., & Ridley, J. K. (2021). Two-timescale response of a large Antarctic ice shelf to climate change. *Nature Communications*, *12*(1), 1991. https://doi.org/10.1038/s41467-021-22259-0

Naveira Garabato, A. C., & Forryan, A. (2017). *The Dynamics of the Orkney Passage Outflow (DynOPO)* (Vol. 47). National Oceanography Centre Southampton Cruise Report.

Nicholls, K. W., Makinson, K., & Osterhus, S. (2004). Circulation and water masses beneath the northern Ronne Ice Shelf, Antarctica. *Journal of Geophysical Research*, *109*. https://doi.org/10.1029/2004JC002302

Nicholls, K. W., Østerhus, S., Makinson, K., Gammelsrød, T., & Fahrbach, E. (2009). Ice-ocean processes over the continental shelf of the southern Weddell Sea, Antarctica: A review. *Reviews of Geophysics*, *47*, RG3003. https://doi.org/10.1029/2007RG000250

Nicholls, K. W., Østerhus, S., Makinson, K., & Johnson, M. R. (2001). Oceanographic conditions south of Berkner Island, beneath Filchner-Ronne Ice Shelf, Antarctica. *Journal of Geophysical Research*, *106*(11), 481–492. https://doi.org/10.1029/2000JC000350

Osborn, T. R. (1974). Vertical Profiling of Velocity Microstructure. *Journal of Physical Oceanography*, *4*(1), 109–115. https://doi.org/10.1175/1520-0485(1974)004<0109:vpovm>2.0.co;2

Osborn, T. R. (1980). Estimates of the Local Rate of Vertical Diffusion from Dissipation Measurements. *Journal of Physical Oceanography*, *10*(1), 83–89. https://doi.org/10.1175/1520-0485(1980)010<0083:eotlro>2.0.co;2

Osborn, T. R., & Cox, C. S. (1972). Oceanic fine structure. *Geophysical Fluid Dynamics*, *3*(4), 321–345. https://doi.org/10.1080/03091927208236085

Padman, L., Fricker, H. A., Coleman, R., Howard, S., & Erofeeva, L. (2002). A new tide model for the Antarctic ice shelves and seas. *Annals of Glaciology*, *34*, 247–254. https://doi.org/10.3189/172756402781817752

Paolo, F. S., Fricker, H. A., & Padman, L. (2015). Volume loss from Antarctic ice shelves is accelerating. *Science*, *348*, 327–331. https://doi.org/10.1126/science.aaa0940

Pawlowicz, R., Beardsley, B., & Lentz, S. (2002). Classical tidal harmonic analysis including error estimates in MATLAB using T_TIDE. *Computers & Geosciences*, *28*, 929–937. https://doi.org/10.1016/s0098-3004(02)00013-4

Peters, H., Gregg, M. C., & Toole, J. M. (1988). On the parameterization of equatorial turbulence. *Journal of Geophysical Research*, *93*(C2), 1199. https://doi.org/10.1029/JC093iC02p01199

Peterson, A. K., & Fer, I. (2014). Dissipation measurements using temperature microstructure from an underwater glider. *Methods in Oceanography*, *10*, 44–69. https://doi.org/10.1016/j.mio.2014.05.002

Piccolroaz, S., Fernández-Castro, B., Toffolon, M., & Dijkstra, H. A. (2021). A multi-site, year-round turbulence microstructure atlas for the deep perialpine Lake Garda. *Scientific Data*, *8*(1), 188. https://doi.org/10.1038/s41597-021-00965-0

Reese, R., Gudmundsson, G. H., Levermann, A., & Winkelmann, R. (2018). The far reach of ice-shelf thinning in Antarctica. *Nature Climate Change*, *8*(1), 53–57. https://doi.org/10.1038/s41558-017-0020-x

Rignot, E., Jacobs, S., Mouginot, J., & Scheuchl, B. (2013). Ice-Shelf Melting Around Antarctica. *Science*, *341*(6143), 266–270. https://doi.org/10.1126/science.1235798

Rippeth, T. P., & Inall, M. E. (2002). Observations of the internal tide and associated mixing across the Malin Shelf. *Journal of Geophysical Research*, *107*(C4), 3028. https://doi.org/10.1029/2000JC000761

Ryan, S., Hattermann, T., Darelius, E., & Schröder, M. (2017). Seasonal cycle of hydrography on the eastern shelf of the Filchner Trough, Weddell Sea, Antarctica. *Journal of Geophysical Research*, *122*, 6437–6453. https://doi.org/10.1002/2017JC012916

Ryan, S., Hellmer, H. H., Janout, M., Darelius, E., Vignes, L., & Schröder, M. (2020). Exceptionally warm and prolonged flow of warm deep water toward the filchner-ronne ice shelf in 2017. *Geophysical Research Letters*, *47*(13). https://doi.org/10.1029/2020GL088119

Salehipour, H., Peltier, W. R., & Mashayek, A. (2015). Turbulent diapycnal mixing in stratified shear flows: The influence of Prandtl number on mixing efficiency and transition at high Reynolds number. *Journal of Fluid Mechanics*, *773*, 178–223. https://doi.org/10.1017/jfm.2015.225

Schröder, M. (2018). The Expedition PS111 of the Research Vessel POLARSTERN to the southern Weddell Sea in 2018. *Reports on Polar and Marine Research*, *718*, 1–161. https://doi.org/10.2312/BzPM_0718_2018

Scott, R. M., Brearley, J. A., Naveira Garabato, A. C., Venables, H. J., & Meredith, M. P. (2021). Rates and Mechanisms of Turbulent Mixing in a Coastal Embayment of the West Antarctic Peninsula. *Journal of Geophysical Research: Oceans*, *126*(5). https://doi.org/10.1029/2020JC016861

Shih, L. H., Koseff, J. R., Ivey, G. N., & Ferziger, J. H. (2005). Parameterization of turbulent fluxes and scales using homogeneous sheared stably stratified turbulence simulations. *Journal of Fluid Mechanics*, *525*, 193–214. https://doi.org/10.1017/S0022112004002587

Stewart, A. L., & Thompson, A. F. (2015). Eddy-mediated transport of warm Circumpolar Deep Water across the Antarctic Shelf Break. *Geophysical Research Letters*, *42*(2), 432–440. https://doi.org/10.1002/2014GL062281

Thompson, A. F., Stewart, A. L., Spence, P., & Heywood, K. J. (2018). The Antarctic Slope Current in a Changing Climate. *Reviews of Geophysics*, *56*(4), 741–770. https://doi.org/10.1029/2018RG000624

Timmermann, R., Wang, Q., & Hellmer, H. H. (2012). Ice-shelf basal melting in a global finite-element sea-ice/ice-shelf/ocean model. *Annals of Glaciology*, *53*(60), 303–314. https://doi.org/10.3189/2012AoG60A156

Vachon, P., & Lueck, R. (1984). A small combined temperature-conductivity probe. In *Proc. 1984 STD Conf. and Workshop* (pp. 126–131). Marine Technology Society.

Vernet, M., Geibert, W., Hoppema, M., Brown, P. J., Haas, C., Hellmer, H. H., et al. (2019). The Weddell Gyre, Southern Ocean: Present Knowledge and Future Challenges. *Reviews of Geophysics*, *57*(3), 623–708. https://doi.org/10.1029/2018RG000604

Wåhlin, A. K., Steiger, N., Darelius, E., Assmann, K. M., Glessmer, M. S., Ha, H. K., et al. (2020). Ice front blocking of ocean heat transport to an Antarctic ice shelf. *Nature*, *578*(7796), 568–571. https://doi.org/10.1038/s41586-020-2014-5

Wåhlin, A. K., Yuan, X., Björk, G., & Nohr, C. (2010). Inflow of Warm Circumpolar Deep Water in the Central Amundsen Shelf. *Journal of Physical Oceanography*, *40*, 1427–1434. https://doi.org/10.1175/2010JPO4431.1